Single Spin Coherence in Semiconductors

Maiken H. Mikkelsen, Roberto C. Myers, Gregory D. Fuchs, and **David D. Awschalom**

Contents		

Center for Spintronics and Quantum Computation, University of California, Santa Barbara, California 93106

1. INTRODUCTION

Spins in semiconductors offer a pathway toward integration of information storage and processing in a single material (Wolf *et al.*, 2001). These applications of semiconductor spintronics require techniques for the injection, detection, manipulation, transport, and storage of spins. Over the last decade, many of these criteria have been demonstrated on ensembles of spins. Encoding and reading out spin information in single spins, however, might be considered the ultimate limit for scaling magnetic information. Single spins in semiconductors also provide a solid state analog of atomic physics which may provide a pathway to quantum information systems in the solid state.

As we will see, single spins in semiconductors can be observed in a variety of systems. In general, the spin needs to be localized to a particular region in the host material in order to make it available for study. The confinement can be provided either by a quantum dot (Berezovsky *et al.*, 2006; Besombes *et al.*, 2004; Bracker *et al.*, 2005; Hanson *et al.*, 2007) or by an individual impurity (Epstein *et al.*, 2005; Jelezko *et al.*, 2004; Myers *et al.*, 2008; Rugar *et al.*, 2004; Stegner *et al.*, 2006). Moreover, the confinement also determines the degree and nature of the coupling with the surrounding environment which is critical to the coherence time. In this chapter we focus on three varieties of single spin systems in semiconductors that can be optically probed and manipulated:

- Single electron spins in quantum dots (Section 2)
- Manganese acceptors in GaAs quantum wells (Section 3)
- Nitrogen-vacancy color centers in diamond (Section 4)

All three types of spins are detected using optical signals resolved in time and position. In the first two cases, the conservation of angular momentum allows for both spin-sensitive detection and injection. In the last case, spin-selective transition rates intrinsic to the color center conveniently provide the same abilities. By coupling these techniques with ultrafast optical pulses, it is possible to stroboscopically measure spin dynamics at bandwidths far exceeding state-of-the-art high speed electronics. The optical experiments discussed here are also spatially resolved using high numerical aperture microscope objectives. This reduces the focal spot size, and therefore measurement region, to ~1 μm in diameter or below. Such spatial resolution allows single quantum dots as well as individual impurities to be studied as in Section 2 and 4, respectively.

Section 2 discusses single electron spins in GaAs quantum dots. The single electron spin state can be sequentially initialized, manipulated, and readout using all-optical techniques. The spins are probed using time-resolved Kerr rotation which allows for the coherent evolution of a single electron spin to be observed, revealing a coherence time of ~10 ns at 10 K.

By applying off-resonant, picosecond-scale optical pulses, the spins can be manipulated via the optical Stark effect. Section 3 introduces magnetic ions as spin recombination centers in semiconductor quantum wells. The magnetization of few magnetic ions can be controlled at zero-field for these normally paramagnetic spins and can in principle be extended to the single-ion limit. These spins might be considered the most strongly coupled system in which strong exchange interactions couple the spin state of the magnetic ions to the band carriers. Despite this coupling, we will see that in the ultra dilute limit, magnetic ions exhibit coherence times near 10 ns at liquid He temperatures. Finally, Section 4 describes single nitrogen-vacancy centers in the wide bandgap semiconductor diamond. These spins represent the opposite end of the spectrum with a spin that is relatively uncoupled to the host band structure resulting in record room temperature spin coherence times of >350 μs (Gaebel *et al.*, 2006). This enables traditional magnetic resonance techniques to be used for nitrogen-vacancy (NV) spin manipulation.

## 2. SINGLE ELECTRON SPINS IN QUANTUM DOTS

Semiconductor quantum dots (QDs) may be realized in a variety of ways, for example, by locally depleting a 2D electron gas with gate electrodes, through chemical synthesis and colloidal chemistry, and through self-assembly using molecular beam epitaxy (MBE). Each type of these quantum dot structures opens up a wide range of possibilities and allows for integration into different systems. The focus here is on optical measurements of MBE-grown GaAs QDs at a temperature of 10 K. A single electron spin state in an individual QD is probed using the magneto-optical Kerr effect. This technique allows one to probe the spin nonresonantly and thus minimally disturbing the system. Next, these measurements are extended to directly probe the time dynamics of the electron spin using pulsed pump and probe lasers. Finally, the ultra-fast manipulation of a single electron spin state via the optical Stark effect is discussed.

In these structures the photoluminescence (PL) from individual QDs has been measured for more than a decade (Gammon *et al.*, 1996). For an ensemble of dots, the inevitable size variations result in a spread of emission energies. Probing fewer dots by using small apertures, for example, allows this broad spectrum to be resolved into very narrow ($\sim$100 μeV) PL lines at different energies. An appropriately small aperture or low density of dots such that the PL lines from different dots can be spectrally resolved allows for individual dots to be studied (Gammon *et al.*, 1996). The spin state may then be readout using polarized PL (Bracker *et al.*, 2005; Ebbens *et al.*, 2005) or polarization-dependent

absorption (Högele *et al.*, 2005; Li and Wang, 2004; Stievater *et al.*, 2002). Recently, polarized PL measurements of single electron spins in an applied magnetic field have also been demonstrated revealing information about the spin-lifetime (Bracker *et al.*, 2005). In the optical study of spin coherence, selection rules play a critical role and will briefly be reviewed below.

2.1. Optical selection rules and the Faraday effect

Electron spins in semiconductors may be initialized and readout using polarized light by exploiting the optical selection rules that exist in zinc-blende semiconductors with a sufficiently large spin–orbit coupling, such as GaAs. The band structure of a zinc-blende crystal is shown schematically in Fig. 1.1A, where E_g is the bandgap and Δ is the spin–orbit splitting. The conduction band is twofold degenerate ($S = 1/2$, $S_z = \pm 1/2$) and the valence band fourfold degenerate with the heavy holes ($J = 3/2$, $J_z = \pm 3/2$) and light holes ($J = 3/2$, $J_z = \pm 1/2$). It is critical that the split-off holes are at a lower energy, Δ, such that a pump energy may be chosen where only transitions from the heavy/light holes to the conduction band are allowed. As illustrated schematically in Fig. 1.1B, the selection rules are due to the conservation of angular momentum. The absorption of a circularly polarized photon transfers its angular momentum $L_z = \pm \hbar$ to the spin, and thus can only drive transition with $\Delta L_z = \pm 1$ (see Fig. 1.1B). For example, the absorption of a photon with $l = 1$ only allows transitions from the $J_z = -3/2$ heavy hole and $J_z = -1/2$ light hole. Conveniently, the
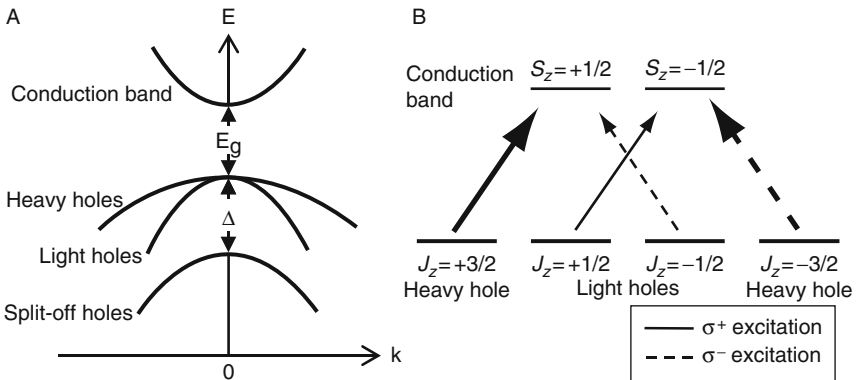
FIGURE 1.1   Band structure and optical selection rules. (A) Schematic of the band structure of a zinc-blende semiconductor. The bandgap, E_g, and the spin–orbit splitting, Δ, are indicated. (B) Optically allowed transitions from the heavy and light hole valence bands ($J = 3/2$) to the conduction band ($S = 1/2$). The thickness of the arrows indicates the strength of the transitions.

heavy hole transition is three times as likely as the light hole transition, which can be shown by calculating the dipole transition matrix elements. This means that three times as many electron spins with $S_z = +1/2$ rather than with $S_z = -1/2$ are injected giving a net spin polarization in the conduction band of 50%. The situation can be improved further if the semiconductor is strained, or if the electrons and holes are confined in one or more dimensions. In this case, the degeneracy of the heavy and light hole bands is lifted, and transitions can be pumped from the heavy hole band only, resulting in ideally 100% conduction band spin polarization.

The inverse process of this optical spin injection provides a means for detecting the spin polarization of carriers in a semiconductor. When an electron and hole recombine, light is emitted with circular polarization that reflects the spin state of the electron and hole. By measuring the degree of circular polarization of this luminescence, one can measure the spin polarization at the time of recombination. Additionally, if the g-factor is known, the spin lifetime can be obtained in a Hanle measurement. Here, the degree of circular polarization of the PL is measured as a function of an applied magnetic field perpendicular to the optically injected spins. The resulting curve has a Lorentzian lineshape, assuming a simple exponential decay process, with a half-width inversely proportional to the product of the g-factor and spin lifetime (Meier and Zakharchenya, 1984). The Hanle effect can even be used to measure the spin lifetime of a single electron spin as shown by (Bracker et al., 2005), where a spin lifetime of 16 ns was observed assuming a g-factor of $\sim$0.2.

A more direct measurement of spin polarization can be obtained through the Faraday effect. Here, a net spin polarization in a material results in a different index of refraction for right and left circularly polarized light. When linearly polarized light is transmitted through the material, the two circularly polarized components acquire a relative phase shift, yielding a rotation of the polarization of the transmitted light. This rotation is proportional to the spin polarization along the direction of light. The Kerr effect is directly analogous, but refers to a measurement made in reflection rather than in transmission. A typical scheme is to use a circularly polarized pump laser to optically inject spins into the conduction band, and a linearly polarized probe laser to measure Faraday (or Kerr) rotation. In this type of pump-probe spectroscopy, the two lasers may have the same or different energies. If the pump and probe lasers are continuous wave (cw) then this provides information about the steady-state spin polarization, similar to the Hanle measurement described above. However, pulsed lasers allow this technique to be extended into the time domain to provide a more direct look at the spin dynamics.

## 2.2. Measuring a single electron spin by Kerr rotation

First, we are interested in the measurement of a single electron spin in a QD using Kerr rotation (KR) with cw pump and probe lasers (Berezovsky *et al.*, 2006). For a single conduction-band energy level in a QD containing a spin-up electron in a state $|\psi_\uparrow\rangle$, optical transitions to the spin-up state are forbidden by the Pauli exclusion principle. Considering only transitions from a single twofold degenerate valence band level $|\psi_{v_0}\rangle$, the KR angle, θ_K, is given by:

$$\theta_K(E) = EC(|P^{\sigma^+}_{\downarrow,v_0}|^2 - |P^{\sigma^-}_{\downarrow,v_0}|^2)\frac{E - E_{0,v_0}}{(E - E_{0,v_0})^2 + \Gamma^2_{0,v_0}} \qquad (1.1)$$

where E is the energy of the probe laser, C is a material-dependent constant, $P^{\sigma\pm}_{c,v} = \langle\psi_c|\hat{p}_x + i\hat{p}_y|\psi_v\rangle$ are the interband momentum matrix elements, E_{0,v_0} is the energy of the transition, and Γ_{0,v_0} is the linewidth of the transition.

For $\Gamma \ll |\Delta| \ll E$, where $\Delta = E - E_0$, we note that the KR angle θ_K, decays slower ($\sim\Delta^{-1}$) than the absorption line ($\sim\Delta^{-2}$) (Guest *et al.*, 2002; Meier and Awschalom, 2005). Therefore, for a suitable detuning, Δ, KR can be detected while photon absorption is strongly suppressed. In a QD containing a single conduction band electron, the lowest-energy interband transition is to the negatively charged exciton state, X$^-$, with an energy E_{X^-}. Thus, a single electron spin is expected to produce a feature in the KR spectrum with the odd-Lorentzian lineshape given by Eq. (1.1), centered at the energy E_{X^-}.

The QDs studied here are MBE-grown simple interface fluctuation QDs, also called natural QDs. They consist of a 4.2 nm GaAs QW where a 2-min growth interruption at each QW interface allows large ($\sim$100 nm diameter; Guest *et al.*, 2002) monolayer thickness fluctuations to develop that act as QDs (Gammon *et al.*, 1996; Zrenner *et al.*, 1994). In addition, the QDs are embedded within a diode structure enabling controllable charging of the dots with a bias voltage (Warburton *et al.*, 2000) (see Fig. 1.2A). The front gate also acts as a shadow mask with 1 μm apertures which are used to isolate single dots as well as to identify the specific position of the dots. The spectrum of the PL as a function of applied bias voltage (Fig. 1.2B) is well established and can therefore be used to identify the different charging states (Bracker *et al.*, 2005). Above 0.5 V, a single line is observed at 1.6297 eV which is caused by recombination from the negatively charged exciton (trion or X$^-$) state. Below 0.5 V, a bright line appears 3.6 meV higher in energy due to the neutral exciton (X^0) transition and in addition, a faint line at 1.6292 eV is visible from radiative decay of the biexciton (XX). To make the measurement of Kerr rotation from a single electron spin easier, the QD layer is centered within an optical microcavity with a resonance chosen to enhance the interaction of the
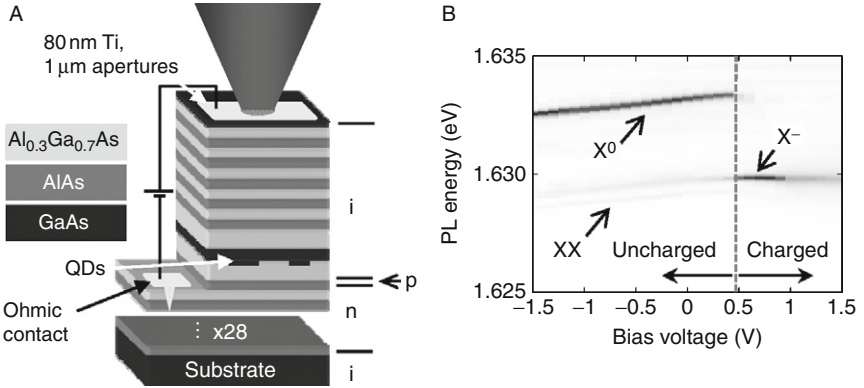
FIGURE 1.2 Sample structure and single dot PL. (A) Schematic of the sample structure. i, n, and p indicate intrinsic (undoped), n-doped, and p-doped regions of the sample, respectively. Twenty-eight repetitions of the AlAs/AlGaAs layers, indicated by × 28, are not shown. (B) PL of a single QD as a function of bias voltage; grayscale indicates PL intensity. A jump in the PL energy indicates the onset of QD charging. Adapted from Berezovsky *et al.* (2006).

optical field with the QD at energies well below the lowest interband transition. The front and back cavity mirrors are distributed Bragg reflectors (DBRs) composed of 5 and 28 pairs of $AlAs/Al_{0.3}Ga_{0.7}As$ $\lambda/4$ layers, respectively (see Fig. 1.2A). This asymmetrical design allows light to be injected into and emitted from the cavity on the same side. The cavity has a quality factor of 120 and an expected enhancement of the KR by a factor of ∼15 at the peak of the resonance (Li *et al.*, 2006; Salis and Moser, 2005). As described above, a circularly polarized pump laser (1.654–1.662 eV) initializes the spins according to the optical selection rules and the spin polarization is verified through polarized PL measurements. To probe spins in the dot through KR, a second, linearly polarized, cw Ti:Sapphire laser is focused onto the sample, spatially overlapping the pump laser. The pump and probe beams are modulated using mechanical choppers, enabling lock-in detection of only spins injected by the pump. Furthermore, at each probe energy the pump excitation is switched between right and left circularly polarized light and the spin-dependent signal is obtained from the difference in the KR angle at the two helicities. The data in Fig. 1.3A show the KR signal and the PL as a function of probe energy at a bias $V_b = 0.2$ V when the QD is nominally uncharged. In this regime, the QD may contain a single spin-polarized electron through the capture of an optically injected electron, or spin-dependent X^- decay. The X^- energy coincides spectrally with a sharp feature observed in the KR data. We can fit these data to Eq. (1.1) including only a single transition in the sum, on top of a broad background (see Fig. 1.3B). The transition
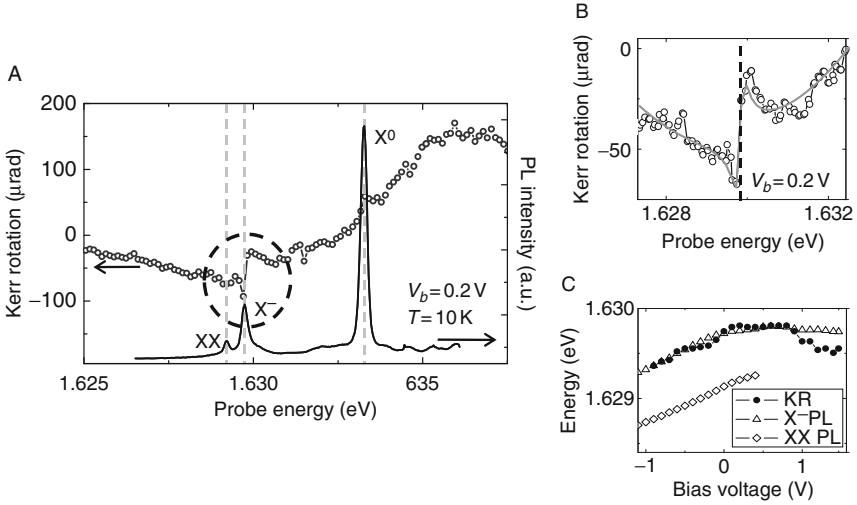
FIGURE 1.3 Single dot KR spectra. (A) KR (open circles) and PL (solid line) spectra at a bias voltage $V_b = 0.2$ V. The circled region is shown in more detail in (B). The solid line indicates a fit to the data and the energy of the X$^-$ PL is indicated by the dashed line. (C) The center of the KR feature, E_0 (solid circles), and the energy of the X$^-$ PL (open triangles) as a function of bias voltage; the two energies show a good agreement. The biexciton (XX) PL energy (open squares) is also shown for comparison. Adapted from Berezovsky *et al.* (2006).

energy E_0, as determined from the fit, is compared to the energy of the X$^-$ PL line as a function of the applied bias in Fig. 1.3C. The two energies agree well and show the same quantum-confined Stark shift. For a single electron spin in the QD ground state, the lowest energy optical transition contributing in Eq. (1.1) is the X$^-$ transition. From these observations we can conclude that the KR feature centered at the X$^-$ energy is indeed from the measurement of a single electron spin in the QD. The measurement has also been repeated on other QDs and the same KR feature at the X$^-$ PL energy has been observed. Additionally, the detection of a single electron spin in InAs QDs has recently been demonstrated using Faraday rotation (Atatüre *et al.*, 2007). The large, broad KR background may be due to transitions involving excited electron and hole states, which are typically a few meV above the lowest transition (Gammon *et al.*, 1996). If present, a KR feature due to the neutral exciton (X^0) spin should appear centered at the biexciton (XX) transition energy. The signal-to-noise in these measurements is not high enough to conclusively identify such a feature. Despite the large amplitude of the X^0 PL compared to the negatively charged exciton (X$^-$) PL in the uncharged bias regime ($\sim$10: 1), the short radiative lifetime of the X^0 state results in a low steady-state X^0 population, and therefore a low KR signal.

2.3. Spin dynamics of a single electron spin

In the experiments described above, only the steady-state spin polarization is measured, concealing information about the evolution of the spin state in time. However, using time delayed pump and probe pulses allows for the spin to be initialized and readout at different times, hence the coherent dynamics of the spin in the QD can be mapped out (Mikkelsen *et al.*, 2007). For this a mode-locked Ti:Sapphire laser provides pump pulses with energy 1.653 eV, and duration $\sim$150 fs at a repetition period $T_r = 13.1$ ns. The bandwidth of the spectrally broad pump pulses is narrowed to $\sim$1 meV by passing the pump beam through a monochromator. The probe pulses are derived from a wavelength tunable cw Ti: Sapphire laser passing through an electro-optic modulator (EOM), allowing for electrical control of the pulse duration from cw down to 1.5 ns. This technique yields short pulses while maintaining the narrow linewidth and wavelength tunability of the probe laser. Also, it allows one to adjust the pulse duration so as to maintain enough average power to achieve good signal-to-noise, while keeping the instantaneous power low enough to avoid unwanted nonlinear effects. The EOM is driven by an electrical pulse generator triggered by the pump laser, allowing for electrical control of the time delay between the pump and the probe pulses. Additionally, in measurements with pump-probe delay of $\Delta t > 13$ ns, the pump beam has also been passed though an electro-optic pulse picker to increase the repetition period of the pulse train to $T_r = 26.2$ ns. For a fixed delay between the pump and the probe, the KR angle, θ_K, is measured as a function of probe energy. At each point, the pump excitation is switched between right and left circularly polarized light, as before, and the spin-dependent signal is obtained from the difference in θ_K at the two helicities. The resulting KR spectrum is fit to Eq. (1.1) plus a constant vertical offset, y_0. The amplitude, $\theta_0 = CE(|P^{\sigma^+}_{\downarrow,v_0}|^2 - |P^{\sigma^-}_{\downarrow,v_0}|^2)\Gamma^{-1}_{0,v_0}$, of the odd-Lorentzian is proportional to the projection of the spin in the QD along the measurement axis. By repeating this measurement at various pump-probe delays, the evolution of the spin state can be mapped out.

When a magnetic field is applied along the z-axis, transverse to the injected spin, the spin is quantized into eigenstates $|\uparrow\rangle$ and $|\downarrow\rangle$, with eigenvalues $S_z = \pm\hbar/2$. The pump pulse initializes the spin at time $t = 0$ into the superposition $|\psi(t=0)\rangle = (|\uparrow\rangle \pm |\downarrow\rangle)/\sqrt{2}$, for $\sigma\pm$ polarized excitation. If isolated from its environment, the spin state then coherently evolves according to $|\psi(t)\rangle = (\exp(-i\Omega t/2)|\uparrow\rangle \pm \exp(i\Omega t/2)|\downarrow\rangle)/\sqrt{2}$, where $\hbar\Omega = g\mu_B B_z$ is the Zeeman splitting. When the probe arrives at time $t = \Delta t$, the spin state is projected onto the x-axis, resulting in an average measured spin polarization of $\langle S_x(\Delta t)\rangle = \pm(\hbar/2)\cos(\Omega \cdot \Delta t)$. This picture has not included the various environmental effects that cause spin

decoherence and dephasing, inevitably leading to a reduction of the measured spin polarization with time. The single spin KR amplitude as a function of delay, measured with a 3-ns duration probe pulse and a magnetic field $B_z = 491$ G, is shown in Fig. 1.4A, exhibiting the expected oscillations due to the coherent evolution described above. Figure 1.4B–F shows a sequence of KR spectra at several delays, and the fits from which the solid black data points in Fig. 1.4A are obtained. In the simplest case, the evolution of the measured KR amplitude can be described by an exponentially decaying cosine:

$$\theta(\Delta t) = A \cdot \Theta(\Delta t) \cdot \exp\left(-\Delta t / T_2^*\right) \cos(\Omega \cdot \Delta t) \qquad (1.2)$$

where A is the overall amplitude, Θ is the Heaviside step function, and T_2^* is the effective transverse spin lifetime (though this measurement eliminates ensemble averaging, the observed spin lifetime may be reduced from the transverse spin lifetime, T_2, by inhomogeneities that vary in time). To model the data, the contributions from each pump pulse
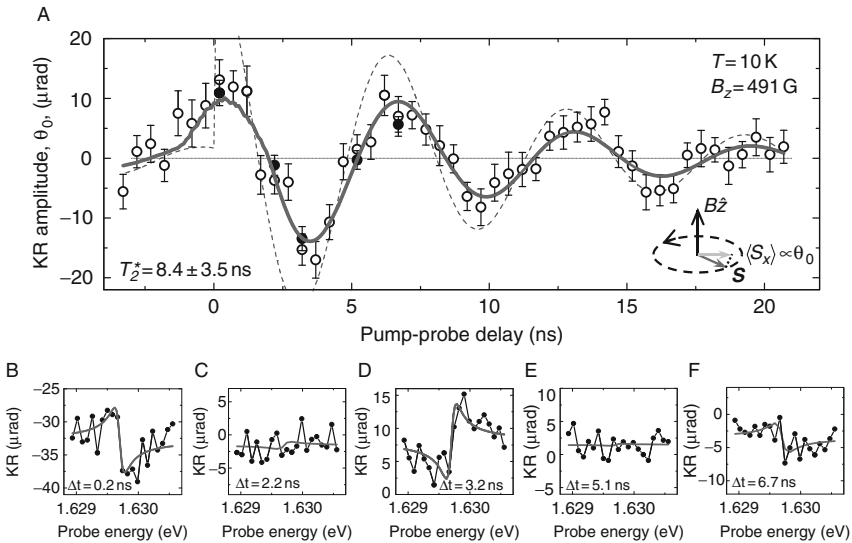

FIGURE 1.4 Coherent evolution of a single electron spin. (A) Single-spin KR amplitude, θ_0, as a function of time with 3-ns duration probe pulses and $B_z = 491$ G. The solid line is a fit to Eq. (1.3) and the dashed line shows Eq. (1.3) without the probe pulse convolution, plotted with the same parameters for comparison. The error bars indicate the standard error as obtained from the least-squares fit to the KR spectra. The solid circles indicate the values of θ_0 obtained from the fits shown in B–F. (B–F) KR angle as a function of probe energy at five different delays; solid lines are fits to the data. Adapted from Mikkelsen *et al.* (2007).

separated by the repetition period T_r are summed and convolved (denoted "*") with the measured probe pulse shape, $p(t)$:

$$\theta_0(\Delta t) = p^* \left[\sum_n \theta(\Delta t - nT_r) \right] \qquad (1.3)$$

The solid line in Fig. 1.4A is a fit to Eq. (1.3), yielding a precession frequency $\Omega = 0.98 \pm 0.02$ GHz and $T_2^* = 8.4 \pm 3.5$ ns. The dashed line shows Eq. (1.3) without the probe pulse convolution, plotted with the same parameters for comparison. In Fig. 1.5A, the precession of the spin is shown at three different magnetic fields and as expected, the precession frequency increases with increasing field. The solid lines in Fig. 1.5A are fits to Eq. (1.3), and the frequency obtained from such fits is shown in Fig. 1.5B as a function of magnetic field. A linear fit to these data yields an electron g-factor of $|g| = 0.17 \pm 0.02$, consistent with the range of g-factors for these QDs found in previous ensemble or time-averaged measurements (Bracker et al., 2005; Gurudev-Dutt et al., 2005). At zero external magnetic field, as shown in Fig. 1.5C, the data fits well to a single exponential decay and the spin lifetime is found to be
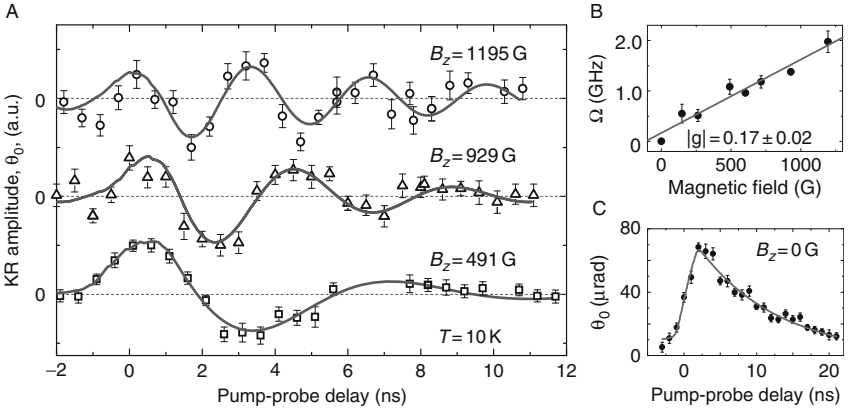
FIGURE 1.5   Magnetic field dependence. (A) Single-spin KR amplitude, θ_0, as a function of delay for $B_z = 1195$ G (circles), $B_z = 929$ G (triangles), and $B_z = 491$ G (squares). The probe-pulse duration is 1.5, 1.5, and 2 ns from top to bottom. Solid lines are fits to Eq. (1.3). The data are vertically offset for clarity. (B) Precession frequency, Ω, of the electron spin as a function of the applied magnetic field, as obtained from fits to the data. Each data point is the average of several delay scans of the same QD and the error bars indicate the root-mean-squared deviation of the measured frequencies. (C) KR amplitude, θ_0, as a function of delay at zero applied magnetic field with a 3 ns probe pulse duration. The solid line shows a fit to Eq. (1.3) yielding $T_2^* = 10.9 \pm 0.5$ ns. Adapted from Mikkelsen et al. (2007).

$T_2^* = 10.9 \pm 0.5$ ns. This value agrees with previous time-averaged (Bracker *et al.*, 2005) and ensemble (Dzhioev *et al.*, 2002; Gurudev-Dutt *et al.*, 2005) measurements where the relevant decay mechanism is often suggested to be dephasing due to slow fluctuations in the nuclear spin polarization. However, these polarization fluctuations are not expected to result in a single exponential decay of the electron spin (Khaetskii *et al.*, 2002; Merkulov *et al.*, 2002). This suggests that other decay mechanisms than nuclear spin fluctuations might also be relevant in this case. In these QDs, the electronic level spacing of ~1 meV (Merkulov *et al.*, 2002) is of the same order as $k_B T$ for this temperature range. Therefore, thermally activated or phonon-mediated processes (Erlingsson *et al.*, 2001; Golovach *et al.*, 2004; Khaetskii and Nazarov, 2001; Semenov and Kim, 2004), which yield an exponential decay, might be significant in this regime.

This measurement technique is also sensitive to small nuclear spin polarizations. Ideally there should be no induced steady-state nuclear polarization in this experimental geometry. Since the magnetic field is applied perpendicular to the direction of the optically injected spins, nuclear spins that are polarized by the electron spins precess around the applied field, resulting in zero steady-state polarization. For any misalignment of the pump laser from the perpendicular, however, there is a projection of the spin along the magnetic field, and right (left) circularly polarized light induces a small dynamic nuclear polarization parallel (antiparallel) to the applied magnetic field (Meier and Zakharchenya, 1984; Salis *et al.*, 2001). Because of the hyperfine interaction this acts on the electron spin as an effective magnetic field, increasing (decreasing) the total effective magnetic field, resulting in a slightly different precession frequency for right and left circularly polarized pump excitation. Since each data point is the difference of the KR signal with right and left circularly polarized excitation, a small deviation from perpendicular between the magnetic field and the electron spin yields a measured KR signal:

$$\theta(\Delta t) = A \cdot \Theta(\Delta t) \cdot \exp\left(-\Delta t / T_2^*\right)[\cos((\Omega + \delta)\Delta t) + \cos((\Omega - \delta)\Delta t)] \quad (1.4)$$

where $\delta = g\mu_B \overline{B_{\text{nuc}}}/\hbar$ is the frequency shift due to the steady-state effective nuclear field, $\overline{B_{\text{nuc}}}$. Insight into the build-up time for the dynamic nuclear polarization can be gained by varying the rate at which the pump helicity is switched. This reveals a nuclear polarization saturation time of ~2 s (Mikkelsen *et al.*, 2007), which agrees with what has previously been found in similar QDs (Gammon *et al.*, 2001). Additionally, by measuring the effective magnetic field exerted by the nuclear spins, one can estimate the nuclear spin polarization.

2.4. Ultrafast manipulation using the optical Stark effect

In Section 2.3 it was discussed how the coherent evolution of a single electron spin can be readout. Here we turn our attention to the manipulation of spins. One way to control one or more spins is through the well-known phenomenon of magnetic resonance. By applying an oscillating magnetic field whose frequency matches the spin precession frequency, the spin state can be coherently controlled. This spin control through electron spin resonance (ESR) has recently been demonstrated on a single electron spin, performing complete rotations of the spin state on a time-scale of tens of nanoseconds (Koppens *et al.*, 2006; Nowack *et al.*, 2007). Additionally, a variety of other optical manipulation schemes have been explored on ensembles of spin (Carter *et al.*, 2007; Dutt *et al.*, 2006; Greilich *et al.*, 2007; Wu *et al.*, 2007).

Using ultrafast optical pulses to coherently manipulate the spin state of a single electron is a key ingredient in many proposals for solid-state quantum information processing (Chen *et al.*, 2004; Clark *et al.*, 2007; Combescot and Betbeder-Matibet, 2004; Economou *et al.*, 2006; Imamoglu *et al.*, 1999; Pryor and Flatté, 2006). In the manipulation scheme discussed here (Berezovsky *et al.*, 2008), the optical, or AC, Stark effect is exploited. Through this effect, an intense, nonresonant optical pulse creates a large effective magnetic field along the direction of the light for the duration of the pulse. Since the generation of short optical pulses is easy using mode-locked lasers, the optical Stark effect can be a very useful tool for ultrafast manipulation of spins. The optical Stark effect was first studied in atomic systems in the 1970s (Cohen-Tannoudji and Dupont-Roc, 1972; Cohen-Tannoudji and Reynaud, 1977; Suter *et al.*, 1991) and subsequently explored in bulk semiconductors and in quantum wells (Combescot and Combescot, 1988; Joffre *et al.*, 1989; Papageorgiou *et al.*, 2004). In recent years, the optical Stark effect has been used to observe ensemble spin manipulation in a quantum well (Gupta *et al.*, 2001), and to control orbital coherence in a QD (Unold *et al.*, 2004).

Using perturbation theory, it is found that an optical field with intensity I_{tip}, detuned from an electronic transition by an energy δ, induces a shift in the transition energy:

$$\Delta E \approx \frac{D^2 I_{\text{tip}}}{\delta \sqrt{\varepsilon/\mu}} \tag{1.5}$$

where D is the dipole moment of the transition, and ε and μ are the permittivity and permeability of the material, respectively (Joffre *et al.*, 1989). Because of the optical selection rules, for circularly polarized light, the optical Stark effect shifts only one of the spin sublevels and produces a

spin splitting in the ground state which can be represented as an effective magnetic field, B_{Stark}, along the light propagation direction. By using ultrafast laser pulses with high instantaneous intensity to provide the Stark shift, large splittings can be obtained to perform coherent manipulation of the spin within the duration of the optical pulse (here, $B_{\text{Stark}} \sim 10$ T).

To perform this manipulation, a third beam is needed which is tuned below the exciton transition energy and synchronized with the pump and probe lasers. The third beam, which we will refer to as the tipping pulse, is derived from the same mode-locked Ti:Sapphire laser which provides the pump pulses. The relative time delay between the pump pulse and the tipping pulse is controlled by a mechanical delay line in the pump path. A schematic of the experimental setup is shown in Fig. 1.6A. Thus, we have three synchronized, independently tunable optical pulse trains that are focused onto the sample: the pump, the probe, and the tipping pulse. The circularly polarized tipping pulse (duration ~ 30 ps, FWHM $= 0.2$ meV) is tuned to an energy below the lowest QD transition (see Fig. 1.6B) and is used to induce the Stark shift. Exactly as in the time-resolved measurements, the spin is initialized at time $t = 0$ along the growth direction (y-axis) and then in the case of a transverse magnetic field coherently precesses at the Larmor frequency. At time $t = t_{\text{tip}}$, the tipping pulse arrives and generates an additional spin splitting along the y-axis for the duration of the pulse. During this time, the spin precesses about the total effective field (which is typically dominated by B_{Stark}), and then continues to precess about the static applied field. The probe pulse then measures the resulting projection of the spin in the QD, $\langle S_y \rangle$ at time $t = t_{\text{probe}}$. This sequence is repeated at the repetition frequency of the laser (76 MHz), and the signal is averaged for several seconds for noise reduction. The spin dynamics can be described using a simple model including the effect of nuclear polarization (see Berezovsky *et al.*, 2008). To map out the coherent dynamics of the spin in the QD, KR spectra are again measured as a function of pump-probe delay. Figure 1.7A shows the time evolution of a single spin in a transverse magnetic field with no tipping pulse applied. Each data point is determined from the fit to a KR spectrum at a given pump-probe delay, as in Fig. 1.4A. Convolving the expected spin dynamics with the measured profile of the probe pulse, a least-squares fit to the data can be performed and various parameters determined: Ω, T_2^*, and the effective field from the nuclear polarization, B_{nuc}. The solid curve in Fig. 1.7A shows the result of this fit, and the dashed line is the corresponding plot without the probe pulse convolution. The values obtained from the fit are later used to model the data including the effect of the tipping pulse. The data in Fig. 1.7B show the same coherent spin dynamics as in Fig. 1.7A, but with the tipping pulse applied at $t_{\text{tip}} = 1.3$ ns when the projection of the spin is mainly along the x-axis. The intensity of the tipping pulse is chosen to induce a $\sim \pi$ rotation
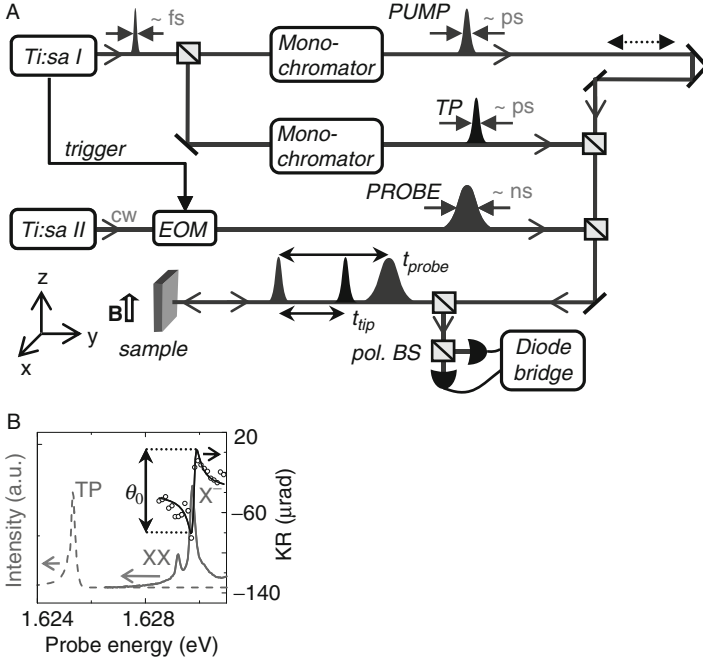
FIGURE 1.6   Setup for spin manipulation using the optical Stark effect. (A) Schematic of the experimental setup; pol. BS = polarizing beam-splitter. (B) The solid gray line shows negatively charged exciton (X^-) and biexciton (XX) PL from a single dot. The black data points show the corresponding single spin KR, and the black line is an odd–Lorentzian fit to this data from which the KR amplitude, θ_0, is obtained. The dashed line shows the tipping pulse (TP) spectrum at a detuning of 4.4 meV. Adapted from Berezovsky *et al.* (2008).

about the y-axis, which is determined as discussed below. After the tipping pulse, the spin has been flipped and the resulting coherent dynamics show a reversal in sign. This can be clearly seen by comparing the sign of the measured signal at the position indicated by the dashed, vertical line in Fig. 1.7. The predicted spin dynamics are shown in the dashed line, and the same curve convolved with the probe pulse is given by the solid line. Note that this curve is not a fit; all of the parameters are determined either in the fit to Fig. 1.7A, or as discussed below. Only the overall amplitude of the curve has been normalized.

 Further details of this spin manipulation can be investigated by varying the tipping pulse intensity, I_{tip}, and the detuning, δ, of the tipping pulse from the QD transition energy for a fixed delay of the tipping and probe pulse as illustrated in Fig. 1.8B. In Fig. 1.8A, the KR amplitude, θ_0, as a function of the tipping pulse intensity is shown at a probe delay of 2.5 ns with the tipping pulse arriving at a delay of 1.3 ns, for three
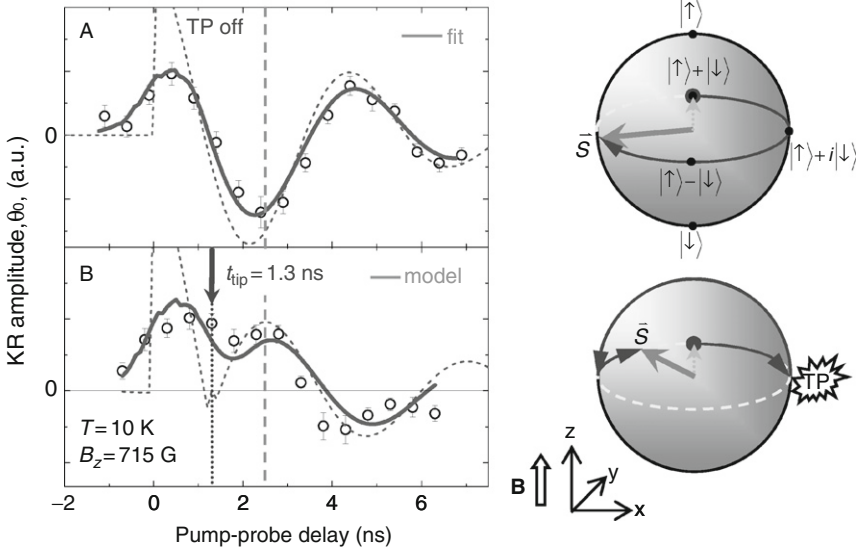
FIGURE 1.7 Ultrafast π rotations of a single spin. (A) Coherent single spin precession in a transverse magnetic field $B_z = 715$ G. The solid line shows a fit to the data, and the dashed line shows the corresponding plot without the probe pulse convolution for the same fit parameters. The diagrams on the right schematically show the evolution of the spin on the Bloch sphere. (B) Spin dynamics under the same conditions as in (A) but with the tipping pulse (TP) applied at $t_{tip} = 1.3$ ns so as to induce a $\sim\pi$ rotation about the *y*-axis. Tipping pulse detuning: $\delta = 2.65$ meV and intensity: $I_{tip} = 4.7 \times 10^5$ W/cm^2. Adapted from Berezovsky *et al.* (2008).

different detunings of the tipping pulse from the transition. When the tipping pulse intensity is zero, the spin precesses undisturbed and yields a negative signal at $t_{probe} = 2.5$ ns as in Fig. 1.7A. As the intensity is increased, the spin is coherently rotated through an increasingly large angle and the observed signal at $t_{probe} = 2.5$ ns changes sign and becomes positive, as in Fig. 1.7B. Furthermore, the strength of the optical Stark effect is expected to decrease linearly as a function of the detuning, as seen in Eq. (1.5). The gray lines in Fig. 1.8A are plots of the predicted spin dynamics with parameters taken from the fit in Fig. 1.7A, and $\phi_{tip} = \beta I_{tip}$. The only parameter that is changed between the three curves in Fig. 1.8A is the strength of the optical Stark effect, β. From this, we can estimate the fidelity of a π-rotation to be $\sim$80%. The tipping pulse intensity required for a π-rotation, $I_\pi = \pi/\beta$, is shown in Fig. 1.8C as a function of detuning, displaying the expected linear dependence.

As explained in the previous section, a small misalignment from perpendicular between the pump beam and the static magnetic field gives rise to a small dynamic nuclear polarization. The data in Fig. 1.8A
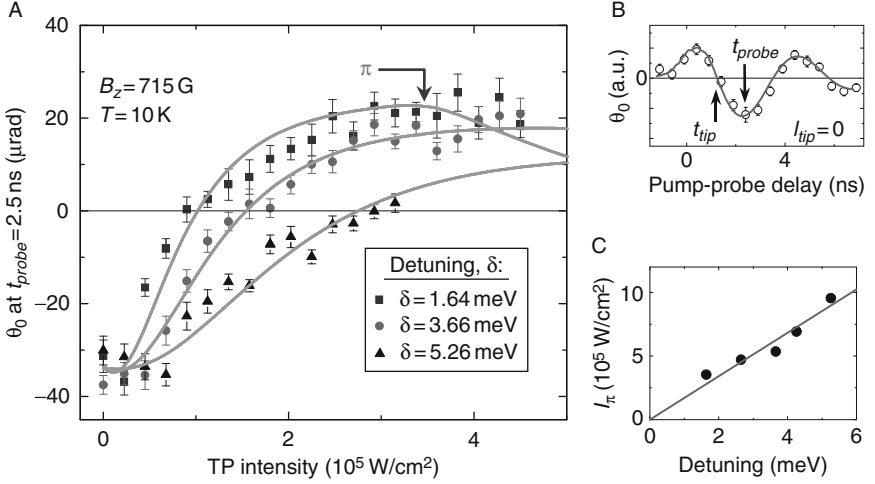
FIGURE 1.8   Intensity and detuning dependence. (A) Single spin KR amplitude, θ_0, as a function of tipping pulse (TP) intensity at three detunings from the X^- transition. The tipping pulse arrives at $t_{tip} = 1.3$ ns, and the probe is fixed at $t_{probe} = 2.5$ ns, as illustrated in (B). The solid gray lines are fits to the data varying only a single parameter, the strength of the optical Stark effect, β. The tipping pulse intensity, I_π, required for a π rotation at $\delta = 1.64$ meV is indicated by the arrow. (C) I_π as a function of detuning, δ, as obtained from the fits. The solid line shows a linear fit to the data. Adapted from Berezovsky *et al.* (2008).

most clearly show the effects of this nuclear polarization on the observed spin dynamics. In the absence of dynamic nuclear polarization, one would expect the curves in Fig. 1.8A to be cosinusoidal, crossing zero at an intensity half that required for a π rotation. Dynamic nuclear polarization however, which is maximal when $\phi_{tip} \approx \pi/2$, distorts this ideal cosine form, as is well described by the model.

2.5. Conclusions

We have described a demonstration of sequential initialization, manipulation, and readout of the state of a single electron spin in a QD using all-optical techniques. First, a single electron spin in a QD is detected using a time-averaged magneto-optical Kerr rotation measurement at $T = 10$ K. This technique provides a means to directly probe the spin off-resonance, thus minimally disturbing the system. Next, this continuous single dot KR technique was extended into the time domain using pulsed pump and probe lasers, allowing observation of the coherent evolution of an electron spin state with nanosecond temporal resolution. The coherent single spin precession in an applied magnetic field directly revealed the electron *g*-factor and a transverse spin lifetime of $\sim$10 ns. Furthermore, the observed spin dynamics provided a sensitive probe of the local nuclear

spin environment. Finally, a scheme to perform ultrafast coherent optical manipulation of a single electron spin state was described. By applying off-resonant, picosecond-scale optical pulses, the coherent rotation of a single electron spin in a QD through arbitrary angles up to π radians was shown. Measurements of the spin rotation as a function of laser detuning and intensity confirmed that the optical Stark effect is the operative mechanism and the results are well described by a model including the electron–nuclear spin interaction.

In principle, at most a few hundred single qubit flips could be performed within the measured spin coherence time. However, by using shorter tipping pulses and QDs with longer spin coherence times, this technique could be extended to perform many more operations before the spin coherence is lost. A mode-locked laser producing ~100-fs-duration tipping pulses could potentially exceed the threshold ($\sim 10^4$ operations) needed for proposed quantum error correction schemes (Awschalom *et al.*, 2002). Additionally, the spin manipulation demonstrated here may be used to obtain a spin echo (Rosatzin *et al.*, 1990), possibly extending the observed spin coherence time. These results represent progress toward the implementation of scalable quantum information processing in the solid state.

3. FEW MAGNETIC SPINS IN QUANTUM WELLS

Detection and control of single magnetic atoms represents the fundamental scaling limit for magnetic information storage. In semiconductors, magnetic ion spins couple to the host semiconductor's electronic structure allowing for bandgap engineering of the exchange interactions (Awschalom and Samarth, 1999). The strong and electronically controllable spin–spin interactions existing in magnetic semiconductors offer an ideal laboratory for exploring single magnetic spin readout and control. The bandgap engineering and electronic control possible in semiconductor heterostructures allows for the localization and control of free carriers over nanometer (nm)-length scales, in particular for quantum wells and quantum dots (see Kaminska and Cibert). Magnetic ions doped within a semiconductor lattice can exhibit relatively long spin lifetimes.

Exploration of single magnetic spins in semiconductors was pioneered in the (II,Mn)-VI system (Besombes *et al.*, 2004). Individual self-assembled ZnSe quantum dots are characterized using microscopically resolved photoluminescence measurements. These quantum dots are doped with Mn-ions at a density such that single magnetic ions occasionally occupy the center of a quantum dot. In these II–VI magnetic semiconductors, the magnetic ions are isoelectronic Mn^{2+} ions with spin-5/2. As will be discussed in later chapters (see Chapters 5 and 9), magnetic spins couple to the host semiconductor through the s–d and p–d exchange with

electron and hole spins, respectively (Furdyna, 1988). The spin state of the magnetic ion is reflected through the exchange splitting of the exciton (electron–hole) spin states. Single magnetic ions in quantum dots are measured via the exchange splitting of the exciton states that results when a single Mn^{2+} ion is centered in the quantum dot. The coupling between exciton and magnetic ions can be controlled electrically by charging the dots with electrons or holes (Leger et al., 2006).

3.1. Mn-ions in GaAs as optical spin centers

A different situation arises in (III,Mn)-V magnetic semiconductors, where the Mn^{2+} ions contribute acceptor states within the bandgap causing the magnetic ions to behave as optical spin centers. As illustrated in Fig. 1.9A, photoexcited electrons in the bottom of the conduction band recombine with holes bound to Mn ions (e, A_{Mn}^0) and emit photoluminescence (PL) (Chapman and Hutchinson, 1967; Schairer and Schmidt, 1974). In GaAs, at low doping levels, the paramagnetic Mn^{2+} ions form a neutral acceptor configuration in which a spin-3/2 heavy hole state is loosely bound and antiferromagnetically coupled to the spin-5/2 Mn^{2+} ion. This neutral acceptor complex (A_{Mn}^0) has a total angular momentum state $J = 1$ and a g-factor $g_{A^0_{Mn}} = 2.77$ measured by electron paramagnetic resonance (EPR) and SQUID magnetometry (Frey et al., 1988; Schneider et al., 1987). This mixing of the Mn ion and valence band states opens the possibility for electrical manipulation of a single magnetic ion even in a bulk crystal (Tang et al., 2006). Individual Mn acceptors can be imaged at surfaces of GaMnAs via scanning tunneling microscopy (STM) as shown in Fig. 1.9B (Yakunin et al., 2004). Alternatively, micro-PL of Mn ions within single quantum wells allows for the spatial isolation of small numbers of Mn ions deep within bandgap engineered heterostructures. An important criterion to observe optical transitions near the bandgap edge in Mn doped GaAs is a proper choice of sample synthesis techniques. The growth technique of choice, MBE allows for atomic layer precision of heterostructures (Gossard, 1986). Most Mn-doped GaAs is grown at low substrate temperatures where defects such as arsenic antisites act as compensating defects and nonradiative traps (Erwin and Petukhov, 2002; Liu et al., 1995). Conversely, at high growth temperatures that are necessary for high quality GaAs/AlGaAs quantum structures, Mn tends to form interstitial defects and MnAs clusters (Ohno, 1998). At intermediate temperatures, a large range of Mn concentrations can be incorporated without forming the unwanted defects. This enables optical measurement of coherent electron spin precession in GaMnAs allowing for a precise measurement of the exchange coupling between electrons and Mn ions (Myers et al., 2005; Poggio et al., 2005).
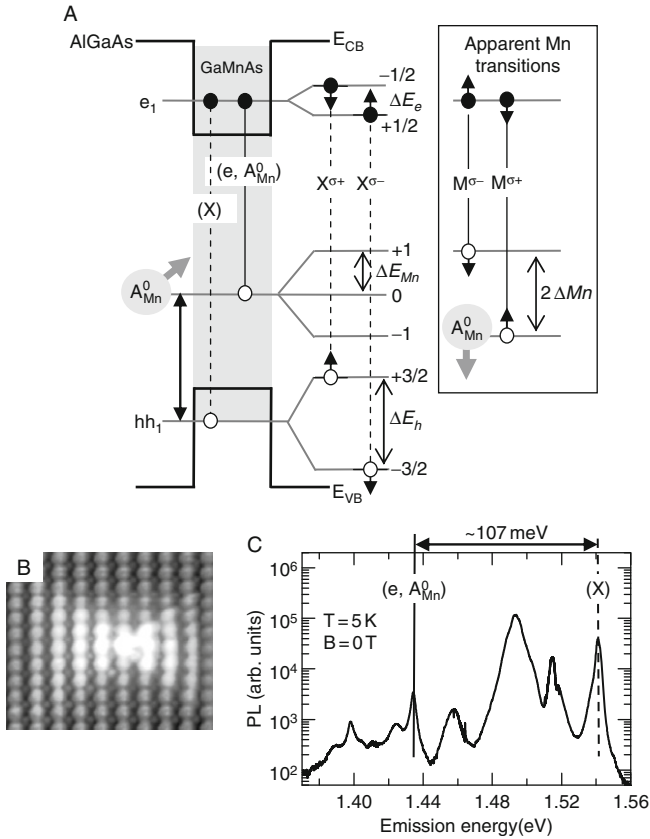
FIGURE 1.9 Optical transitions in (III,Mn-V) quantum wells. (A) Bandedge along the growth direction showing optical transitions of excitons and Mn acceptor emission. In addition to the exciton exchange splitting (ΔE_e and ΔE_h), an apparent spectroscopic splitting of Mn acceptor PL (ΔMn) occurs if the Mn spin states are split by ΔE_{Mn}. (B) Mn acceptors imaged by STM, adapted from Yakunin *et al.* (2004). (C) Full photoluminescence (PL) emission energy spectrum of a Mn:GaAs single QW with Mn doping density of 7.3×10^{18} cm^{-3}. Adapted from Myers *et al.* (2008).

Figure 1.9A shows a schematic of the optical transitions occurring within such Mn-doped quantum wells. As indicated in the PL spectrum (Fig. 1.9C), the Mn acceptor emission (e, A_{Mn}^0) is red-shifted by ~107 meV from the quantum well exciton (X) PL. In bulk, the A_{Mn}^0 state lies ~110 meV above the valence band edge.

Polarization-resolved PL yields the angular momentum of the emitted photons, and through conservation of angular momentum, gives information about the spin state of electrons, holes, and the Mn acceptors. In quantum wells of zinc-blende semiconductors, the optical selection

rules yield optical transitions with specific circular polarity depending on the spin state of the recombining carriers (Meier and Zakharchenya, 1984). Figure 1.9A shows the spin-selective heavy hole exciton (X) transitions in the presence of a spin splitting generated by a positive magnetic field (either real or effective) along the measurement axis and near $k \sim 0$. The boxed region shows the circularly polarized Mn-related optical transitions, which occur due to overlap of the localized Mn acceptor state with the band tail. The circular polarization of the (e, A_{Mn}^0) emission is sensitive to both the spin polarization of the Mn ions and the electrons (Averkiev et al., 1988). The PL from (D^0, A_{Mn}^0) in bulk GaAs has been used to investigate the Mn ion polarization (Karlik et al., 1982; Kim et al., 2005). PL from recombination of hot electrons, away from $k \sim 0$, into the Mn acceptor state was also observed (Sapega et al., 2007). In these measurements, the polarization of the Mn acceptor state was tracked in multiple quantum wells showing a decrease in the polarization with increasing quantum confinement.
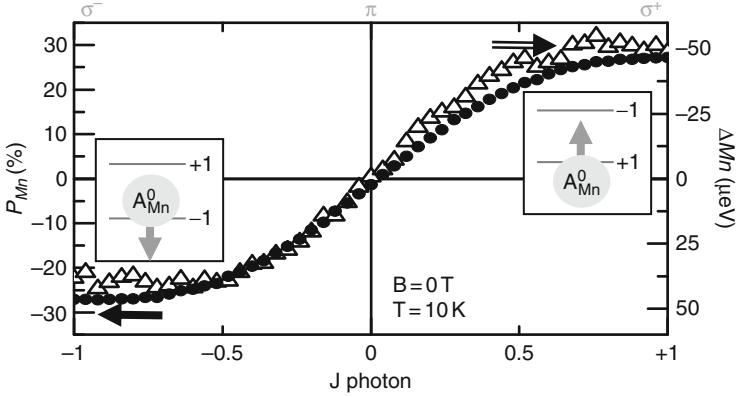
3.2. Zero-field optical control of magnetic ions

An example of the (e, A_{Mn}^0) PL spectra from an Mn-doped GaAs quantum well is shown in Fig. 1.10. The data are taken using a circularly polarized laser tuned to the heavy hole X transition in the quantum well, which injects spin-polarized electrons and holes into the quantum well as shown in the schematic. At zero magnetic field, the polarization resolved spectra show higher intensity for one detection helicity than the other implying a zero-field spin polarization, discussed below. By fitting the spectra to two Gaussians (solid lines), the peak position ($M^{\sigma\pm}$) and intensity ($I_M^{\sigma\pm}$) are extracted from which either a polarization $\left(P_{Mn} = \left(I_M^{\sigma+} - I_M^{\sigma-}\right)/\left(I_M^{\sigma+} + I_M^{\sigma-}\right)\right)$ or spectral splitting ($\Delta Mn = M^{\sigma+} - M^{\sigma-}$) are measured. When a linearly polarized (π) laser is used for excitation, the polarization (P_{Mn}) is zero at zero magnetic field and follows the paramagnetic alignment of Mn ions with longitudinal field (B_z) (Fig. 1.10B). If a $\sigma\pm$ polarized laser is used, the odd symmetry of (P_{Mn}) with magnetic field is broken. For $\sigma+$, the polarization saturates more quickly for $B_z < 0$, and shows slower saturation for positive field. The opposite trend is seen for the opposite helicity excitation. This implies that optical spin injection results in an effective magnetic field on the spin states of the Mn ions, which is positive for $\sigma-$ and negative for $\sigma+$. Such an effective magnetic field should generate a splitting of the Mn acceptor m_J states at zero field, as drawn schematically in Fig. 1.10A, resulting in a spectral splitting of the (e, A_{Mn}^0) emission lines. Such a spectral splitting (ΔMn) is observed at zero field, which traces the polarization (P_{Mn}) (Fig. 1.11).
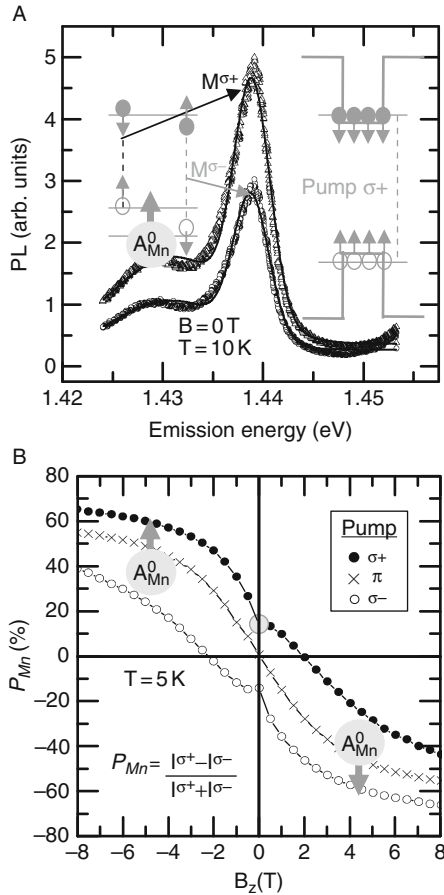
FIGURE 1.10   Optical readout of magnetic ion spin orientation. (A) Polarization-resolved Mn acceptor PL (P_{Mn}). A $\sigma+$ polarized laser injects spin polarized electrons and holes into the quantum well and generates an Mn-ion spin polarization. Solid lines are fits to the data (black points). (B) Longitudinal field (B_z) dependence of the Mn-ion spins. The field symmetry of the Mn paramagnetism under π polarized excitation is broken in the case of optical spin injection ($\sigma\pm$ polarized excitation). Adapted from Myers *et al.* (2008).

The angular momentum of the photons in the excitation beam is tuned by changing the polarization state smoothly from $\sigma-$ to π to $\sigma+$ using an electronically tuned waveplate. The orientation of the Mn-ions tracks the helicity in both polarization and spectral splitting corresponding to the Mn ion spin splitting and orientation shown schematically in Fig. 1.11. The optically induced magnetization, described above, occurs due to optical excitation of spin polarized carriers into the quantum well. By changing the energy of the excitation laser, it is possible to inject different configurations of electron and hole spins into the quantum well and

FIGURE 1.11 Zero-field optical control of magnetic ion spins. The circular polarization (left axis) and the associated spectral splitting (right axis) of the Mn acceptor emission are altered in sign and magnitude as the photon helicity and angular momentum are varied using a variable wave retarder. Adapted from Myers *et al.* (2008).

differentiate their effect on the magnetic ions. Figure 1.12 plots the intensity, polarization, and spectral splitting of the Mn acceptor emission as the laser energy is tuned near the absorption edge of the quantum well for a fixed helicity. At 1.546 eV, the σ+ polarized laser is resonant with the heavy hole exciton absorption generating spin down electrons and spin up heavy holes, as schematically shown. This excitation generates a maximum in the PL intensity of the Mn emission. A second PL maxima occurs at 1.557 eV where the laser coincides with the light hole exciton absorption which generates spin up electrons and light holes in the quantum well. For this resonance, the Mn polarization and spin splitting change sign compared to the heavy hole resonance. Thus, the orientation of the Mn spins at zero field is changed by tuning the laser excitation energy.

For a given photon helicity, the sign of the electron spin changes between the heavy and light hole exciton transitions, while the hole spins are parallel. This is drawn schematically in Fig. 1.12. Thus, the change in sign of the Mn ion polarization between the heavy and light hole transitions cannot occur due to interaction with holes alone, but rather the sign change implies that electron–Mn spin interaction generates the nonequilibrium magnetization.

3.3. Mechanism of dynamic polarization and exchange splitting

We now discuss how such a zero-field magnetization is possible in GaAs. For magnetic semiconductors, the mean-field interaction between charge carrier and magnetic ion spins is the so-called (s−d) and (p−d)
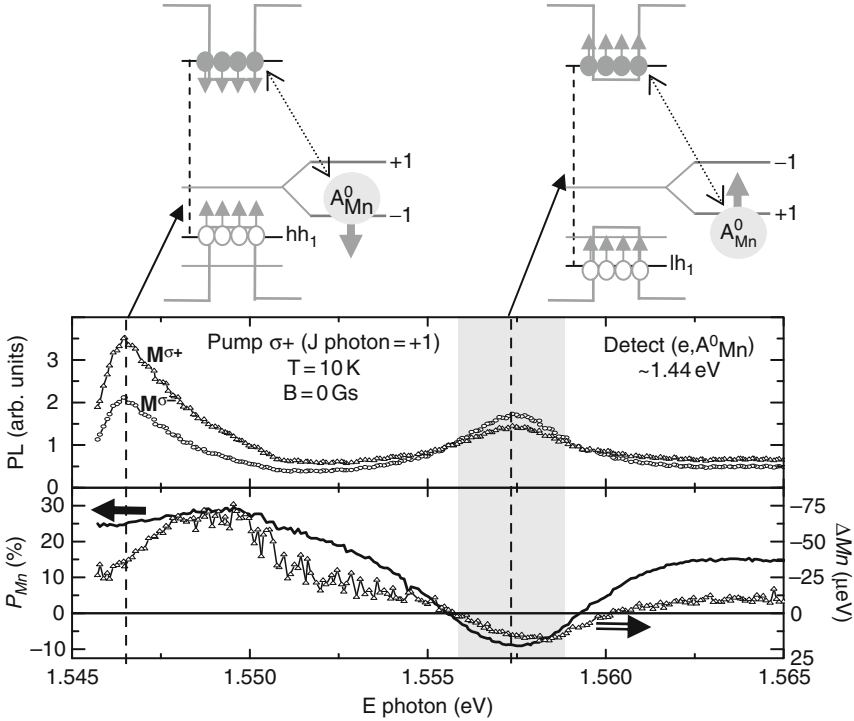
FIGURE 1.12   Photon energy dependence of the dynamic magnetic polarization. The photon helicity is fixed and its energy is varied. The detection energy is fixed at the Mn acceptor emission line. Optically injected electron spins change sign between the heavy hole (hh) and light hole (lh) exciton resonances and generate a change in sign of the Mn spin polarization and exchange splitting. Adapted from Myers *et al.* (2008).

exchange interactions between conduction and valence band spins and the magnetic ions (Dietl, 1994). The Mn spin splitting due to the s, p−d exchange coupling is the sum of both terms:

$$\Delta E_{\mathrm{Mn}}^{\mathrm{s,p-d}} = n\alpha\langle S_{\mathrm{e}}\rangle + p\beta\langle S_{\mathrm{h}}\rangle \tag{1.6}$$

where n and p are the optically excited electron and hole densities, and $\langle S_{\mathrm{e}}\rangle$ and $\langle S_{\mathrm{h}}\rangle$ are the electron and hole spin average values, respectively. When spin polarized electrons and holes are optically injected, $n\langle S_{\mathrm{e}}\rangle$ and $p\langle S_{\mathrm{h}}\rangle$ take on finite values. The data shown in Fig. 1.12 are taken using a pump power generating at most $n = p = 4 \times 10^{17}$ cm^{-3} electrons and holes spin polarized with $\langle S_{\mathrm{e}}\rangle = 1/2$ and $\langle S_{\mathrm{h}}\rangle = 3/2$. The average exchange field they exert on the magnetic ions decays with the spin lifetime of the carriers, where electron spins in these structures have measured spin

lifetimes of $\sim$100 ps (described below) and hole spins have spin lifetimes of $\leq$1 ps (Damen *et al.*, 1991). These parameters yield $\Delta E_{Mn}^{s,p-d} \leq 2\mu eV$. Thus, the s, p$-$d exchange field is too weak by more than an order of magnitude to explain the observed polarization and spin splitting ($\Delta Mn \sim 50$ μeV). The observed zero-field splitting of the Mn ion spin states originates from interactions with neighboring Mn ions. This is surprising considering the low doping level at which the effect is observed, corresponding to many atomic distances between Mn ions. Qualitatively, the loosely bound hole of the neutral Mn acceptor allows for longer range interactions between Mn spins than is otherwise possible. The interaction between neutral Mn acceptors has been treated using multi-band tight binding model of the Mn acceptor wave function (Tang and Flatté, 2004). This model has successfully predicted the shape of the acceptor wave function as imaged via scanning tunneling microscopy (Fig. 1.9B) and the interactions between pairs of Mn acceptors (Kitchen *et al.*, 2006). Using this model, the mean field effect of all the Mn ions in the crystal can be calculated which contributes an additional spin splitting to the Mn spin states:

$$\Delta E_{Mn} = \Delta E_{Mn}^{s,p-d} + \lambda \langle J_{Mn} \rangle \tag{1.7}$$

where λ is the Weiss molecular field due to neighboring Mn ions and $\langle J_{Mn} \rangle$ is the projection of angular momentum of the Mn ion along the magnetic field. λ is calculated by summing the interaction with neighboring Mn spins, yielding energy splittings that vary from 0.01 μeV for 6×10^{17} Mn/cm^3 to 400 μeV for 7×10^{18} Mn/cm^3 (Myers *et al.*, 2008). We now have a clear picture of how paramagnetic Mn ions become magnetized by spin injection. Electron–Mn spin interaction initiates a polarization of the Mn spins generating a finite $\langle J_{Mn} \rangle$. Once they are partially aligned, the Mn–Mn mean field interaction favors a parallel orientation of Mn spins and generates an exchange splitting as in Eq. (1.7).

3.4. Spin dynamics of Mn-ions in GaAs

Because Mn spins can be optically oriented at zero field, we can apply a transverse field (B_x) to precess the spins about the applied field. The time-averaged spin precession and decay is observed as a decrease in the PL polarization as the field is increased (Fig. 1.13A) called the Hanle effect:

$$P(B_x) = \frac{P(0)}{\left(g\mu_B B_x T_2^* / \hbar \right)^2 + 1} \tag{1.8}$$
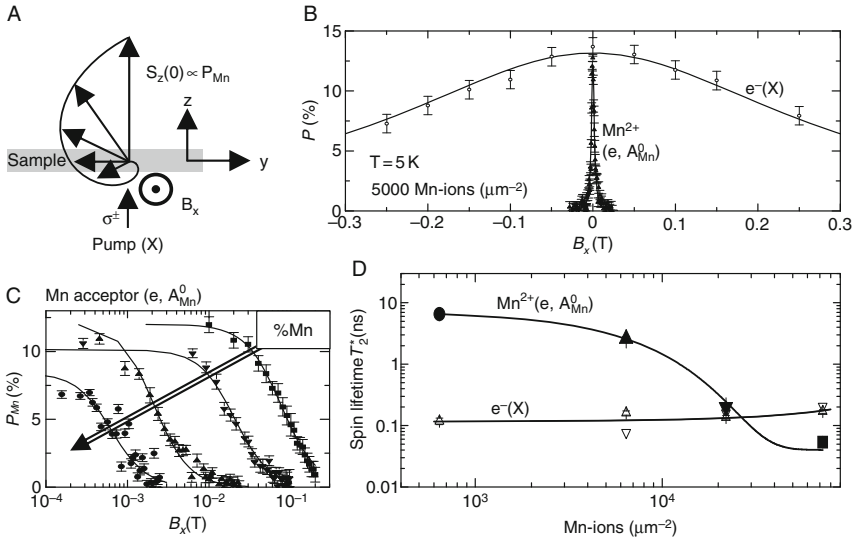
FIGURE 1.13 Spin lifetime measurement of Mn ions and electron spins. (A) Hanle effect measurement of time-averaged spin precession in a transverse field (B_x). (B) Hanle curves from the exciton PL (open circles) and the Mn acceptor emission (solid triangles), sensitive to the electron and Mn spin precession, respectively. (C) Hanle measurement of the Mn spin precession for samples with different Mn density. Lines in (B) and (C) are fits to Eq. (1.8). (D) Spin lifetime (T_2^*) of the Mn ions (closed) and the electrons (open) extracted from Hanle data are plotted as a function of Mn concentration. Lines guide the eye. Adapted from Myers *et al.* (2008).

and $1/T_2^* = 1/\tau_r + 1/\tau_s$, where T_2^* is the effective transverse spin lifetime of the spin ensemble, τ_r is the recombination lifetime and τ_s is the spin relaxation time (Meier and Zakharchenya, 1984). If the g-factor of the precessing spin is known, then the lifetime can be extracted. Electron spin precession in the QW is observed by measuring polarization of the (X) emission versus transverse field showing the Hanle effect. In a similar fashion, Mn spin precession is observed from Hanle measurements of the Mn acceptor emission. As seen in Fig. 1.13B, the Mn-related Hanle curve has a width at least one order of magnitude narrower than the electron (X)-related Hanle curve. From Eq. (1.8), this implies that gT_2^* for Mn acceptors is 10 times larger than for electrons in this particular QW. As the Mn density is reduced, a dramatic narrowing of the Hanle curves is observed, shown in a semi log plot in Fig. 1.13C. The g-factor of the electrons is known from optical measurements of these structures (Stern *et al.*, 2007), and the g-factor of the neutral Mn acceptor is known to be $g_{A^0_{Mn}} = 2.77$ (Schneider *et al.*, 1987) allowing the spin lifetimes to be extracted. These values are plotted in Fig. 1.13D as a function of the Mn ion density within single 10-nm thick GaAs quantum wells.

Using micro-PL technique, the collection spot is narrowed to a 1 μm diameter spot allowing for small numbers of Mn ions to be probed. Below 20,000 Mn ions within the detection spot, the spin lifetime dramatically increases and saturates near 10 ns at the lowest doping levels corresponding to the detection of several hundred magnetic ions within a square micron. This reflects the effect of inhomogeneous Mn–Mn spin interactions that dephase the spins. In contrast, electron spins maintain a roughly 100 ps lifetime over all Mn densities.

3.5. Conclusions

Micro-PL within single quantum wells provides a method to isolate small numbers of Mn ion emittors, which is scalable to the single ion limit. When spins are injected into the quantum well, a unique spin scattering mechanism generates zero-field, nonequilibrium polarization and magnetization of Mn ions even though they are paramagnetic at equilibrium. Optically induced magnetism in II–VI materials usually arises due to the mean field interaction of the ions with the electron and hole spins. In the case of Mn ions doped in GaAs, the neutral acceptor state results in a unique system where both electron–Mn and Mn–Mn interactions come into play and generate a dynamic exchange splitting of the magnetic ions. Mn ion spin coherence lifetimes can be at least as long as those of electron spins in quantum dots, allowing us to consider single Mn ion spins in III–V's as potentially useful for storage and readout of spin information. Because bandgap engineering is very well developed, a whole host of interesting structures for engineering the charge and spins of single Mn ions in GaAs-based heterostructures is possible.

4. SINGLE SPINS IN DIAMOND

4.1. Introduction

Diamond as a wide bandgap semiconductor has a number of useful and interesting properties including high mobilities (Isberg *et al.*, 2002) and excellent thermal conductivity (Wei *et al.*, 1993). Typical semiconducting diamond is p-type, with boron being the principle dopant. The most common impurity in diamond, however, is substitutional nitrogen that forms an impurity level ~1.7 eV below the conduction band (Farrier, 1969). Additionally, these nitrogen spins can form a different defect when they occur on a lattice site next to a vacancy (Fig. 1.14A). These defect centers, known as NV centers, are optically active single spins with robust quantum properties that extend up to room temperature. In this
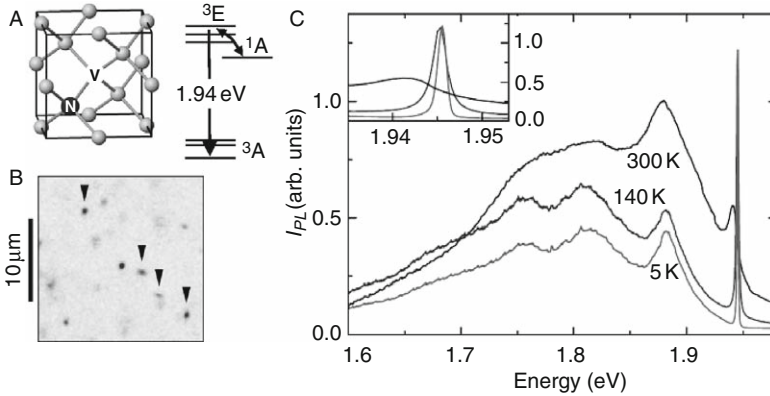
FIGURE 1.14 (A) A unit cell of the diamond lattice containing an NV center. The solid line connecting the nitrogen substitutional defect to the neighboring vacancy shows the symmetry axis of the NV center. Also shown is a summary diagram of the electronic levels of the NV center. (B) A spatial image of the photoluminescence intensity plotted using a linear gray scale. Several individual NV centers are marked. (C) An energy resolved photoluminescence spectra of an ensemble of NV centers at three temperatures. (Inset) Close-up of the zero phonon line. (A) and (B) are taken from Epstein *et al.* (2005) and (C) is taken from Epstein (2005).

section we will discuss diamond NV centers as individually addressable single spins that may form the basis for room temperature quantum information systems.

4.2. NV basics

An NV center can be thought of as a "solid-state" molecule with discrete energy levels inside the 5.5 eV gap of diamond. The electronic wave function is mainly centered on the dangling bonds of the carbon atoms adjacent to the vacancy, with very little overlap with the N nucleus (He *et al.*, 1993). This results in a very small hyperfine splitting of the electronic spin levels due to the contact hyperfine interaction. Figure 1.14A shows a schematic of the electronic energy levels, including the ground state (^{3}A), the excited state (^{3}E), and a metastable spin singlet state (^{1}A) with intermediate energy (Nizovtsev *et al.*, 2003). The electronic ground state (^{3}A) is a spin triplet (e.g., $S = 1$) with a zero-field splitting $D = 2.87$ GHz between the $m_s = 0$ and $m_s = \pm 1$ levels (Loubser and van Wyk, 1978; Nizovtsev *et al.*, 2003). At zero applied field, the $m_s = \pm 1$ levels are degenerate in unstrained diamond, but they become Zeeman split in an externally applied magnetic field. The spin is quantized along the symmetry direction which is set by the orientation of the NV symmetry axis ($\langle 111 \rangle$) within

the crystal lattice (Loubser and van Wyk, 1978). The excited state (^{3}E) is also a spin triplet but determination of its structure is an ongoing investigation (Manson and McMurtrie, 2007). The ^{3}A→^{3}E transition is phonon broadened at room temperature, with only a small portion of the photons emitted due to the direct transition (1.94 eV) known as the zero phonon line (ZPL). The ZPL, however, becomes much more prominent at low temperature (Fig. 1.1C) (Clark and Norris, 1971; Epstein, 2005).

Although the dipole allowed optical transitions between ^{3}A and ^{3}E are spin conserving (i.e., $\Delta m_s = 0$) in unstrained diamond, optical pumping polarizes the NV spin into the $m_s = 0$ state (Harrison *et al.*, 2004). This is due to the presence of a spin-selective intersystem crossing. Transitions between ^{3}E and ^{1}A are dipole forbidden but still occur out of the $m_s = \pm 1$ states due to the spin–orbit interaction (Manson *et al.*, 2006). Once in the ^{1}A state, the system eventually relaxes into the ground state. After several cycles, the probability for the spin to be in the $m_s = 0$ spin state will be high. In addition, since the ^{3}E→^{1}A transition is nonradiative, the NV center's PL rate under optical excitation is smaller when the spin is in the $m_s = \pm 1$ than when it is in the $m_s = 0$ state. This means the spin state of a single NV center can be determined by measuring the relative PL intensity. It should be noted, however, that measurements require illumination which, given enough time and intensity, will repolarize the spin and lose the spin information.

One major feature of diamond NV centers is that they can be imaged with confocal fluorescence microscopy techniques on an individual basis. Figure 1.14B shows an image of a region in a synthetic type 1b diamond that contains several individual NV centers. The image was taken with a scanning confocal microscope, using a 100 × objective with a numerical aperture of 0.73 and linearly polarized 532 nm light that is focused ∼1 μm below the diamond surface. Since the focal spot is nearly diffraction-limited, individual NV centers can be resolved if they are spaced by more than ∼1 μm. Although there is some thermal drift in the sample position over time on this length scale, using feedback loop tracking enables extended measurements of a single NV center for days or longer.

To insure that an individual NV center is being addressed rather than several at once, we use the fact that they are single-photon emitters. Using time correlated single photon counting we can measure the time-dependent auto-correlation function of the emitted photons. A schematic of the setup is shown in Fig. 1.15A. The PL intensity, I_{PL}, from the NV center(s) are passed through a nonpolarizing 50:50 beam-splitter in the Hanbury–Brown–Twiss arrangement and collected in two separate avalanche photo diode photon detectors. If there is only one NV center present, then at $t = 0$, the normalized autocorrelation function, $g^{(2)}(\tau) = \langle I_{PL}(\tau)I_{PL}(t + \tau)/I_{PL}(t)^2 \rangle$ will approach zero (Becker, 2005). This effect is
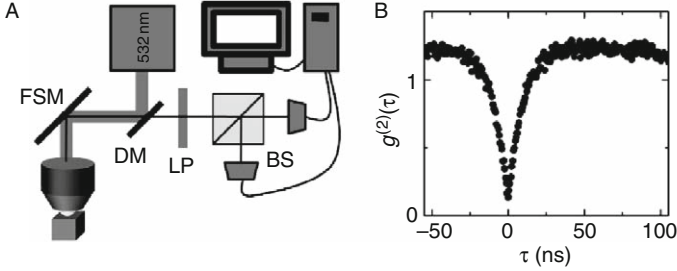
FIGURE 1.15 (A) Schematic of experimental apparatus used to study single NV centers. The abbreviated labels are: FSM = fast steering mirror, DM = dichroic mirror, LP = long pass filter, and BS = 50:50 nonpolarizing beam-splitter. In addition, the detectors are silicon avalanche photo-diodes that are connected to computer-based data acquisition. (B) A plot of the photoluminescence intensity correlation function $g^{(2)}(\tau)$ versus *tau* for NV1. The dip below $g^{(2)}(\tau) = 0.5$ indicates that the photons are emitted from a single source. (B) is taken from Epstein *et al.* (2005).

known as anti-bunching and is the signature of a single-photon emitter. Anti-bunching data for a single NV center is shown in Fig. 1.15B (Epstein *et al.*, 2005).

4.3. Anisotropic interactions of a single spin

As mentioned previously, the symmetry axis of an NV center also determines its quantization axis. The Hamiltonian of the NV spin in the electronic ground state is:

$$H_{NV} = g_e \mu_B \vec{B} \cdot \vec{S}^{\,NV} + D[(S_z^{NV})^2 - S^{NV}(S^{NV} + 1)/3] + \vec{S}^{\,NV} \bar{A}^{NV} \vec{I}^{\,NV} \quad (1.9)$$

where $g_e = 2.00$ is the electron g-factor, μ_B is the Bohr magneton, $\vec{B}$ is the magnetic field and $\vec{S}$ is the NV center spin, and D is the 2.87 GHz zero-field splitting (Charnock and Kennedy, 2001; Loubser and van Wyk, 1978). S_z for a single NV center is along one of the [111] crystal orientations. In addition, the last term in Eq. (1.9) describes the hyperfine interaction between the NV center electronic spin and the nuclear spin of the nitrogen. The components of $\bar{A}$ are a few MHz (He *et al.*, 1993). Using this Hamiltonian, we can calculate the eigen-energies for different magnetic field orientations. This is plotted in Fig. 1.3B for the angle $\theta = 6°$ and $54.7°$, where θ is the angle between $\vec{B}$ and the [111] direction (neglecting the hyperfine term). When θ is nonzero, there are spin mixing terms in H_{NV}. Near $B = 1000$ G this causes a level avoided crossing (LAC) between $m_s = -1$ and $m_s = 0$ spin states. When θ is small, the spin mixing is only significant at fields near the LAC, while large values of θ create spin mixing even at fields far from the LAC (Epstein *et al.*, 2005). This spin

mixing can be seen in Fig. 1.16B where $|\alpha|^2$, the overlap of the each eigenstate with $|0\rangle$, which we define as the $m_s = 0$ spin state in the [111] basis, is plotted against B for the same two field angles. The other coefficients are given by $|m_s\rangle = \alpha|0\rangle + \beta|-1\rangle + \gamma|+1\rangle$ in that basis. Measurements of I_{PL} as a function of B can be used to investigate the spin mixing effects. Figure 1.16B plots these data for three different NV centers with B oriented $1°$ from [111]. NV1 shows two dips, one near $\sim$1000 G and another near $\sim$500 G. The $\sim$1000 G dip can be attributed to the LAC previously mentioned, while the $\sim$500 G dip has a different origin that we will address later. The PL intensities for NV2 and NV3 are significantly reduced as the field increases and show no other features above $B = 200$ G. The intensity is reduced due to enhanced spin mixing which indicates that these NV centers have one of the other $\langle 111\rangle$ orientations (Epstein *et al.*, 2005).

For NV centers that are aligned with [111], the width of the PL dip at $\sim$1000 G depends sensitively on the angle between B and [111] (Fig. 1.16D and E) (Epstein *et al.*, 2005). As $\theta\rightarrow 0°$, the LAC dip becomes narrower, which indicates decreased spin mixing, and is consistent with the Hamiltonian in Eq. (1.9). While the LAC dip disappears altogether for some NV centers (e.g., NV4; Fig. 1.16E), this is not always the case. This residual spin mixing even at nearly perfect alignment can be attributed to strain and nuclear interactions (He *et al.*, 1993), which can vary from center to center.

The LAC can be modeled as a pseudo spin-$1/2$ system for small values of θ. With B near the LAC, the $|+1\rangle$ state can be ignored since it has almost no overlap with $|0\rangle$ (i.e., see Fig. 1.16B). In this case, we can rewrite Eq. (1.9) as $H = g\mu_B(\vec{B} - \vec{B}_o)\vec{s}$ where $\vec{B}_o$ cancels the zero-field splitting and $\vec{s}$ is a spinor. Then, the Bloch equations for $\vec{B}$ in the $(1\bar{1}0)$ plane are taken to be:

$$\frac{ds_x}{dt} = -\Omega_z s_y - \frac{s_x}{T_2}$$

$$\frac{ds_y}{dt} = \Omega_z s_x - \Omega_x s_z - \frac{s_y}{T_2} \qquad (1.10)$$

$$\frac{ds_z}{dt} = \Omega_x s_y - \frac{s_z}{T_1} + \Gamma$$

where $\hbar\vec{\Omega} = g\mu_B(\vec{B} - \vec{B}_o)$, $\hbar$ is the reduced Plank's constant and $\vec{\Omega}$ is the Larmor vector, T_1 is the longitudinal (spin-flip) relaxation time while T_2 is the transverse (dephasing) relaxation time (Epstein *et al.*, 2005). Γ is the rate of optical polarization of the NV center, which is included since the
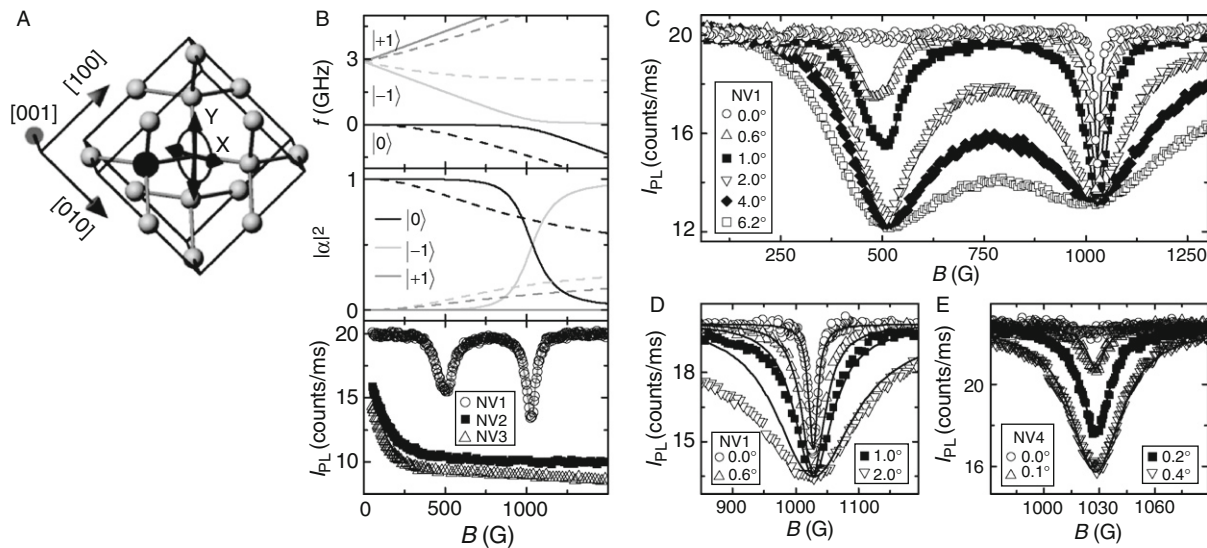
FIGURE 1.16   (A) Schematic of the measurement dipole transition X and Y. (B) Upper panel: Eigen-energies in frequency units (GHz) as a function of magnetic field for $\theta = 6°$ (solid lines) and $\theta = 54.7°$ (dashed lines). Middle panel: Overlap $|a|^2$ for each spin level with $|0\rangle$ at the same two angles. (C) I_{PL} versus magnetic field at several angles for NV1. (D) Close-up of the data for B near 1000 G (points) for several angles along with fits (lines) to the model described in the text. (E) I_{PL} versus magnetic field at several angles (points) for NV4, along with fits (lines). This figure is modified from Epstein *et al.* (2005).

measurements are made under continuous illumination. Therefore, T_1 and T_2 depend on Γ as $(T_1)^{-1} = (T_z)^{-1} + 2\Gamma$ where T_z is the intrinsic longitudinal relaxation time, and there is a similar expression for T_2 (Epstein *et al.*, 2005). Figure 1.16 illustrates the coordinate system, which is fixed relative to the lattice. Here we use $x \,||\, [\overline{1}\,\overline{1}2], y \,||\, [1\overline{1}0]$, and $B_o \,||\, z \,||\, [111]$. Experimentally, the photoluminescence intensity I_{PL} can be related to the spin projection s_z. The steady-state solution for s_z is (Epstein *et al.*, 2005):

$$s_z = \frac{T_1\Gamma\left(1 + \Omega_z^2 T_2^2\right)}{1 + \Omega_x^2 T_1 T_2 + \Omega_z^2 T_2^2} \tag{1.11}$$

Furthermore, this model can be used to directly model the experimental data by taking $I_{PL} = An_0 + Bn_{-1} = A(1/2 + s_z) + B(1/2 + s_z)$. Here A and B are the photon emission rates from the $|0\rangle$ and $|-1\rangle$ spin states, respectively. Equation (1.11) combined with this simple model of the photoluminescence describes the $B \sim 1000\,\text{G}$ LAC data over a large range of angles. In addition, fits to the model can be used to extract lifetime for NV4 $T_1 = 64$ ns and $T_2 = 11$ ns using a laser power of 2.9 mW (Epstein *et al.*, 2005). The large PL dip at ~ 500 G has origins that are not described by the ground-state spin Hamiltonian. This feature is observed in all the NV centers that were studied when suitably aligned with the [111] direction. This dip is a very broad feature, which suggests that it is related to a fast relaxation process. One possibility is that there is a LAC in the excited state of the NV center at this field and orientation. If that is the case, then using a similar analysis to the one described above for the ~ 1000 G LAC yields a $T_1 = 36$ ns and a $T_2 = 1.8$ ns for this state (Epstein *et al.*, 2005).

Near the broad 500 G dip there are also signs of the NV center interacting with its environment. For every NV center in the diamond, there are 10^6–10^8 more nitrogen spins in these nitrogen rich type-Ib diamonds. The nitrogen impurities have electronic spin 1/2 and nuclear spin 1 (for ^{14}N) but are not optically active and hence "dark" to a direct optical probe. Nevertheless, these spins are present and interact with the NV center spin through dipolar coupling. The Hamiltonian for the nitrogen spins is:

$$H_N = g_N \mu_B B S_z^N + S^N \overline{A}^N I^N \tag{1.12}$$

where S^N is the nitrogen electronic spin, I^N is the nitrogen nuclear spin, $g_N = 2.00$ is the g-factor of the nitrogen electronic spin, and $\overline{A}$ is the nitrogen hyperfine tensor. The NV to N electronic dipolar coupling Hamiltonian is (Hanson *et al.*, 2006b; Slicter, 1990):

$$H_{\text{dip}} = \frac{\mu_o g_{\text{NV}} g_N \mu_B^2}{4\pi r^3} \left[\vec{S}^{\text{NV}} \cdot \vec{S}^{\text{N}} - 3 \left(\vec{S}^{\text{NV}} \cdot \hat{r} \right) \left(\vec{S}^{\text{N}} \cdot \hat{r} \right) \right]. \qquad (1.13)$$

Figure 1.17A compares the spin-splitting as a function of magnetic field for both the NV centers and for an N electronic spin for *B* parallel to [111]. At 514 G, the spin splitting is the same for both of these spin species, and hence resonant coupling between the N spin bath and an NV center is possible for sufficiently high N concentrations (e.g., small enough value of $\langle r \rangle$). This dipolar interaction, therefore, creates another LAC at 514 G, which accounts for the PL dip observed at that field. Including the hyperfine interaction of the N electronic spin with its nuclear spin, the nitrogen levels are split into three (Fig. 1.17B), for $m_I = -1$, 0, and +1. Hence, there are actually three LACs, which can be observed separately for small values of θ (Fig. 1.17C) (Hanson *et al.*, 2006b).
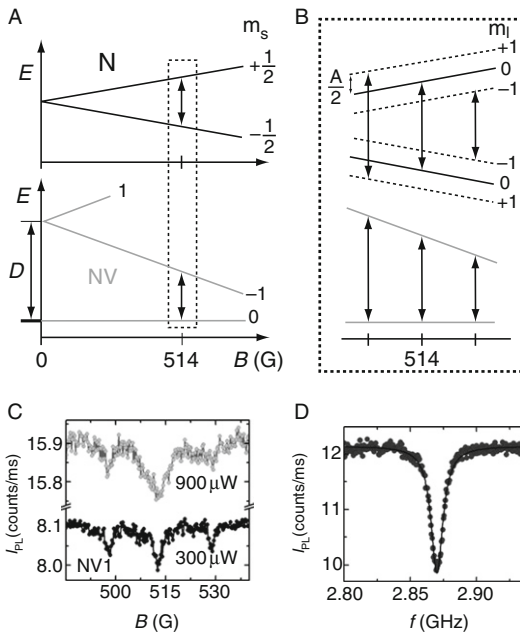
FIGURE 1.17 (A) Energy diagram versus magnetic field for the spin levels in nitrogen and NV centers. At 514 G, the spin splitting is the same for both centers. (B) Close-up of the energy diagram including the hyperfine splitting for ^{14}N. (C) I_{PL} versus magnetic field for NV1 at two laser powers where additional LACs due to the hyperfine splitting of N are evident as satellite dips. (D) I_{PL} versus frequency of applied microwave radiation. The PL dip is the result of a resonant spin transition. (A) and (B) are taken from Hanson *et al.* (2006b) and (C) and (D) are taken from Epstein *et al.* (2005).

4.4. Single NV spin manipulation and coherence

The techniques of ESR and nuclear magnetic resonance (NMR) that were developed for spin ensembles (Slicter, 1990) are also effective for single spin measurements. As with traditional ESR, the spin is manipulated with a microwave frequency magnetic field B_{rf}, but here the spin state is detected optically by measuring the PL intensity. When the microwave field is resonant with the spin splitting, the spin will undergo Rabi nutations. In order to understand these affects, it is helpful to think about the spin dynamics in a rotating reference frame (Slicter, 1990). In the lab frame without B_{rf}, the spin precesses about the static field at the Larmor frequency given by the energy splitting between the spin levels ΔE, or $f_L = \Delta E/h$, where h is the Plank's constant. By transforming into the reference frame that is rotating at f_L, the spin is static. When B_{rf} is applied, it appears as a static field in the rotating frame, and the spin's dynamic response is to precess[1] about B_{rf}. In this way, the spin can be manipulated between the various spin states, including coherent superpositions of the states.

The probability $P_{|0\rangle}$ of finding the spin in the $|0\rangle$ state will then be given by Rabi's formula (Sakurai, 1994):

$$P_{|0\rangle} = 1 - \frac{f_1^2}{f_1^2 + \Delta f^2} \sin^2\left(\pi\sqrt{f_1^2 + \Delta f^2}\right)t \tag{1.14}$$

where f_1 is the Rabi frequency, Δf is the detuning from the resonant frequency, and t is the time. The Rabi frequency depends on the amplitude of the B_{rf} as $f_1 = g\mu_B B_{rf}/(2h)$, where h is the Plank's constant. In addition, the overall oscillation decays as $e^{-t/T_2'}$ where T_2' is the inhomogeneous[2] dephasing time which is typically shorter than T_2, the transverse relaxation time.

ESR is easiest to observe in the frequency domain by continuously illuminating the NV center while sweeping the frequency f of B_{rf}. This measurement produces a dip in the PL signal as f approaches f_L since $\langle P_{|0\rangle}\rangle$ falls as the NV spin undergoes continuous oscillations between $|0\rangle$ and the other spin state on the time scale of the measurement (recall: the photon emission rate is highest for $|0\rangle$). Away from the resonance, the continuous illumination polarizes the spin into $|0\rangle$. Figure 1.17D shows typical ESR data taken of a single NV center for the $|0\rangle \rightarrow |\pm1\rangle$ transition.

In the time domain, spin resonance is also known as Rabi oscillations, which is a direct measurement of the coherent evolution of the NV spin

---

[1] This is why we previously used the term nutation. In the lab frame, the spin dynamics include both the Larmor precession about the static field, and also a "wobble" due to the dynamical response to B_{rf}.

[2] Since we are measuring a single spin rather than an ensemble of spins, it might seem like we should use T_2 rather than T_2'; however, the need for signal averaging in the measurement means the signal is still sensitive to inhomogeneous broadening in time rather than in space as for an ensemble measurement.

under a resonant microwave drive. The measurement requires a pump-probe cycle that is outlined in Figure 1.18A. First, the laser illuminates the NV center for several microseconds in order to initialize it into the $|0\rangle$ state, after which the illumination is turned off using an acousto-optic modulator. Then, after letting the NV center relax into the electronic ground state (^{3}A) for 2–3 µs, a pulse of microwave radiation of varying lengths is applied. Finally, the spin state is read out with a short (2–3 µs) laser pulse during which I_{PL} is measured. This cycle is repeated many ($\sim 10^5$) times for each microwave pulse duration in order to build up statistics. Figure 1.18B shows a plot of I_{PL} as a function of microwave pulse duration for a single NV spin with three different values of microwave power (Hanson *et al.*, 2006a). Each trace fits well to Eq. (1.14) with a single f_1 that is proportional to the square root of the microwave power. The oscillations in Fig. 1.18B decay with values of T_2' on a microsecond time scale.

In order to study the factors that contribute to T_2', Rabi measurements were performed to determine T_2' over a broad range of magnetic fields. The results are summarized in Fig. 1.18C and D (Hanson *et al.*, 2006a). Most striking is the sharp peak in $1/T_2'$ located at 514 G that is evident in Fig. 1.18C. Figure 1.18D shows additional $1/T_2'$ data taken at fields near to 514 G. The fields where increases in $1/T_2'$ are observed closely track the PL dips that occur due to LACs where the NV and N levels are resonant.
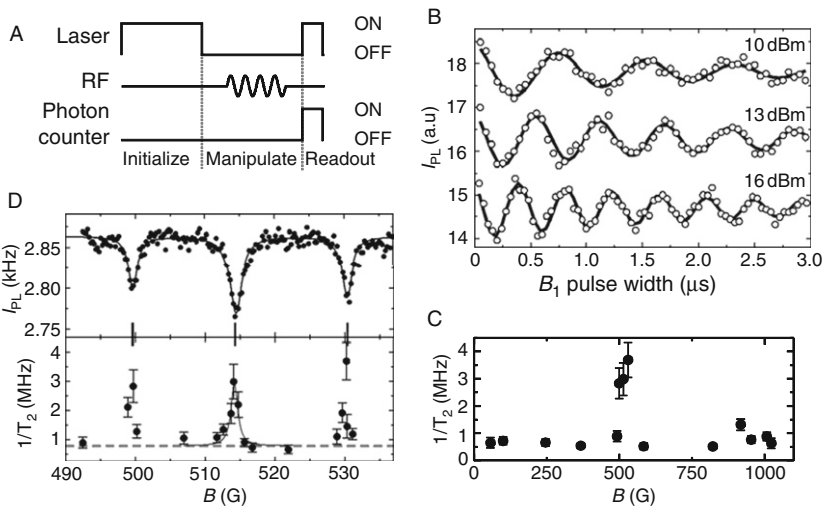
FIGURE 1.18 (A) Timing diagram that illustrates the pump-probe sequence used to measure Rabi oscillations. (B) Rabi oscillations plotted for NV14 for three values of the applied microwave power. (C) $1/T_2'$ plotted as a function of magnetic field. These data show increases in $1/T_2'$ at the fields where there is a LAC. (D) Close-up of $1/T_2'$ data near the 514 G LAC. Figures modified from Hanson *et al.* (2006a).

This strongly suggests that fluctuations in the N spins as they interact with the NV spin is an important source of decoherence (Hanson *et al.*, 2006a).

Another interesting feature of the Rabi data in Fig. 1.18B is that the T_2' also depends on the microwave power. This suggests that there is a refocusing effect, where a long microwave pulse can be viewed as a series of π-pulses (Hanson *et al.*, 2006a; Vandersypen and Chuang, 2005). If true, then the transverse relaxation time T_2 is longer than T_2' due to dephasing caused by the environment of the NV spin. This was further investigated by using a Hahn spin-echo pulse sequence as outlined in Fig. 1.19A rather than a single microwave pulse. In this scheme, first a π/2-pulse brings the NV spin coherently into the $1/\sqrt{2}(|0\rangle + |-1\rangle)$ state. Then there is a period τ_1 of free evolution of the spin during which dephasing can occur. This is followed by a π-pulse which introduces a 180° phase shift so that the state is nominally $1/\sqrt{2}(|0\rangle - |-1\rangle)$ which is followed by another free evolution period, τ_2. Finally, another π/2-pulse is applied to bring the spin back to $|0\rangle$ for measurement of the state. If there is low-frequency dephasing that occurs during τ_1, it will occur with the opposite sign during τ_2, leading to a refocusing of the spin coherence (Slicter, 1990). First, this was checked by measuring I_{PL} as τ_2 was varied. It was found that there was a peak in I_{PL} at $\tau_1 = \tau_2 = \tau$ (Fig. 1.19B), which indicates that there are low-frequency interactions with the environment that cause dephasing of spin during the Rabi measurement. These effects reduce the nominal coherence time of the NV spin. Then, the Hahn echo at $\tau_1 = \tau_2 = \tau$ was measured as a function of τ, which is shown in Fig. 1.19C along with a fit to an exponential decay. The decay of the signal gives the value of T_2, which for this NV center is 6 μs. As expected, this is significantly longer than typical values of T_2' (see Fig. 1.18C) (Hanson *et al.*, 2006a).
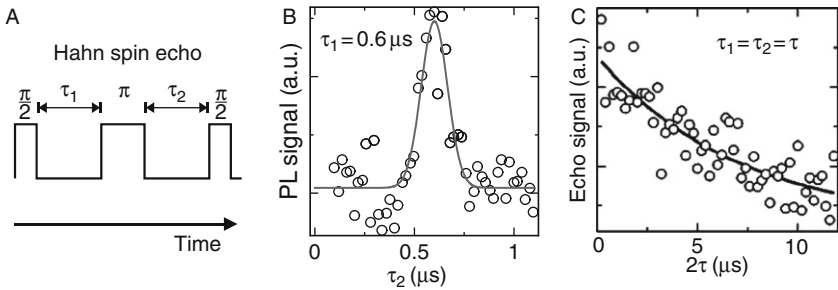
FIGURE 1.19   (A) Timing diagram of the spin echo pulses used in the Hahn measurement. (B) Plot of the PL signal versus τ_2 for a Hahn measurement where $\tau_1 = 0.6$ ms. The solid line is a guide to the eye. (C) Plot of the PL signal taken during a Hahn measurement where $\tau_1 = \tau_2 = \tau$. The data is fit to an exponential decay (solid line) giving a value of $T_2 = 6$ ms. (A) and (C) are modified from Hanson *et al.* (2006a).

4.5. Coupled spins in diamond

Previously, we have been addressing measurements and manipulations of a single NV electronic spin. These measurements have suggested that the spin environment created by a number of weakly coupled nitrogen spins has a major impact on the coherence properties of the NV center. Alternatively, the NV center may be strongly coupled to a single nitrogen spin, with dynamic properties that are dominated by the coupling (Gaebel *et al.*, 2006; Hanson *et al.*, 2006b).

In that situation, the ESR peak in the frequency domain is split by an amount proportional to the strength of the coupling (Fig. 1.20C and D). Since they are coupled by the dipolar interaction, the splitting depends strongly on the distance due to the factor of $1/r^3$ in Eq. (1.13). We can understand the splitting in terms of a local magnetic field exerted by the N spin. Away from the 514 G LAC, the spin projections (m_s^{NV} and m_s^N) remain good quantum numbers. Each of the two ESR peaks are due to the $|0\rangle \rightarrow |-1\rangle$ transition of the NV spin, but they occur at different frequencies depending on whether m_s^N is $+1/2$ or $-1/2$. That is because the nitrogen spin exerts a dipolar field $\vec{B}_{dip}$ on the NV center that depends on the relative position of the two spins with respect to their quantization axis.
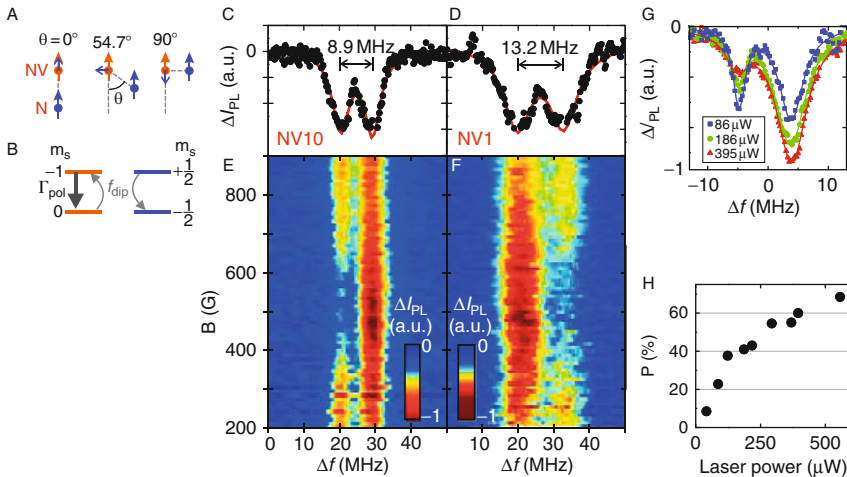
FIGURE 1.20 (A) Schematic diagram showing the direction of B_{dip} for an NV center coupled with a single N defect for the limiting cases of $\theta = 0°$, 54.7°, and 90°. (B) Energy diagram of the spin dynamics that results from dipolar coupling between an NV center and an N spin. (C) and (D) show ESR spectra taken as a function of B for NV10 and NV1, respectively. The spectra for each value of B are concatenated and plotted with a 2D color scale (E) and (F). (G) Plot of ESR spectra for three different values of laser illumination. (H) Plot of polarization versus laser power. Figure is modified from Hanson *et al.* (2006b)

In this case, the NV center has a fixed quantization axis along [111] and the nitrogen's axis is set by the external field which is also aligned to the [111] direction. Figure 1.20A outlines the possibilities for the coupling. If the angle θ between the [111] direction and $\vec{r}$ is small (e.g., the spins are lined up front-to-back), then when the spins align with the external field, $\vec{B}_{\mathrm{dip}}$ from the nitrogen is also aligned with the external field, making the total field on the NV center larger. If, on the other hand, θ is similar to $90°$ (e.g., the spins are lined up side-by-side) then $\vec{B}_{\mathrm{dip}}$ is anti-aligned with the external field. As θ varies between these two angles, there is an increasing component perpendicular to the quantization axis, with $\theta = 54.7°$ being the ''magic angle'' where $\vec{B}_{\mathrm{dip}}$ is exactly at $90°$ with respect to the NV spin orientation (Hanson *et al.*, 2006b; Slicter, 1990). If θ is exactly at $0°$ or $90°$, $\vec{B}_{\mathrm{dip}}$ is parallel to the applied field, and there is no LAC between the NV and N eigenstates, with the only effect being to adjust the total field magnitude on the NV center. At angles in between, however, the spin levels of the NV center and N become mixed at the resonance condition ($B = 514$ G) to form a LAC (Hanson *et al.*, 2006b). The NV center spin and the N spin can then undergo a spin flip-flop (Fig. 1.20B). Under continuous illumination, the NV center is polarized in $|0\rangle$ with the rate Γ_{pol}. Therefore, since the NV center is being preferentially driven into $|0\rangle$, the majority of the flip-flops will be to take the NV from $|0\rangle \rightarrow |-1\rangle$ and the N from $|+1/2\rangle \rightarrow |-1/2\rangle$. This results in the PL decrease associated with the LAC noted previously (e.g., see Fig. 1.17C and 1.18D).

Figure 1.20E and F shows ESR scans of two different NV centers (NV1 and 10) taken as a function of magnetic field and plotted together to form a 2D contour plot (Hanson *et al.*, 2006b). As the applied field approaches the resonance point, one of the two ESR peaks disappears. This is the result of the flip-flop process described above, indicating that the peak that disappears is the $|+1/2\rangle$ state of N (Gaebel *et al.*, 2006; Hanson *et al.*, 2006b). This data also allows us to learn something of the angle θ between each of these NV centers and their respective N. The ESR peak that disappears for NV10 is at a lower frequency (Fig. 1.7E) indicating that $\vec{B}_{\mathrm{dip}}$ tends to decrease the field magnitude for the $|+1/2\rangle$ state and therefore θ must be close to $90°$. The peak that disappears for NV1, however, is at higher frequency so the opposite must be true; θ must be near to $0°$. Given the sign of the coupling for each of these NV centers, it is possible to estimate the upper limit of the NV–N separation using Eq. (1.13) to be 2.3 nm for NV10 and 2.6 nm for NV1 (Hanson *et al.*, 2006b).

Since the N spins are being polarized due to flip-flops with the NV center, the polarization of the N spins should also be proportional to the polarization rate Γ_{pol} of the NV center under illumination. This was investigated by measuring the ESR spectra for different values of the laser power. The data is plotted in Fig. 1.20G. As the laser power increases, the difference in the amplitude change, ΔI_{PL}, of the two peaks

became greater. By fitting to the amplitudes, one can explicitly calculate the polarization of the N using:

$$P = \frac{\Delta I_{\mathrm{PL}}(-1/2) - \Delta I_{\mathrm{PL}}(+1/2)}{\Delta I_{\mathrm{PL}}(-1/2) + \Delta I_{\mathrm{PL}}(+1/2)} \tag{1.15}$$

where P is the N polarization and $\Delta I_{\mathrm{PL}}(\pm 1/2)$ is the PL change in the optically detected ESR feature for $m_s^{\mathrm{N}} = \pm 1/2$ (Hanson *et al.*, 2006b). The results, plotted in Fig. 1.20H, show that the polarization becomes saturated near 70% as the rate of optical polarization is balanced against spin-relaxation processes (Hanson *et al.*, 2006b). These measurements show a pathway toward initialization of coupled spins, which is an important measure of control for quantum information purposes.

4.6. Conclusions and outlook

The long spin lifetimes at room temperature (Gaebel *et al.*, 2006; Kennedy *et al.*, 2003), coupled with the ability to optically initialize and readout the spin state of diamond NV centers, make this system a strong candidate for applications in quantum information. Furthermore, they are quickly becoming a standard choice of room temperature, single-photon sources (Kurtsiefer *et al.*, 2000) for applications in quantum optics. There have also been a number of theoretical proposals to use NV centers for decoherence free quantum computing (Brooke, 2007), quantum repeaters (Childress *et al.*, 2006b), and quantum teleportation (Gottesman and Chuang, 1999) to name a few.

Recent observations of the coherent dynamics of NV centers coupled with individual nearby spins suggest a pathway toward useful room temperature quantum computers with multiple coupled qubits. These include N electronic spins as discussed here (Gaebel *et al.*, 2006; Hanson *et al.*, 2006b) and ^{13}C nuclear spins (Childress *et al.*, 2006a; Dutt *et al.*, 2007; Jelezko *et al.*, 2004). Moreover, in the case of the coupled NV-^{13}C spin system, simple quantum computing gates have been successfully implemented, including a ''CROT'' gate (Jelezko *et al.*, 2004) and a ''swap gate'' (Dutt *et al.*, 2007).

One of the major challenges for the development of such quantum computers is the scaling of NV center-based qubits. Although nearby spins with sufficient coupling occur naturally, the probability of their formation is low. Not only does this make the likelihood of finding an NV center spin system composed of 3, 4, or 5 spin-based qubits prohibitively small, but it also essentially rules out the possibility of scaling to large arrays of coupled spins. Progress, however, has also been made on this front as well. Meijer and colleagues (Meijer et al., 2005; Rabeau *et al.*, 2006) have successfully created regular arrays of single NV centers with

the accuracy of 0.3 μm using ion implantation techniques. Although this level of control is not yet sufficient to customize the interaction between NV centers and surrounding spins, it is an important first step in scaling and engineering NV centers in diamond for quantum information applications.

REFERENCES

Atatüre, M., Dreiser, J., Badolato, A., and Imamoglu, A. (2007). *Nat. Phys.* **3,** 101–105.

Averkiev, N. S., Gutkin, A. A., Osipov, E. B., and Reshchikov, M. A. (1988). *Sov. Phys. Solid State* **30,** 438.

Awschalom, D. D., and Samarth, N. (1999). *J. Magn. Magn. Mater.* **200,** 130–147.

Awschalom, D. D., Loss, D., and Samarth, N. (2002). ''Semiconductor Spintronics and Quantum Computation.'' Springer-Verlag, Berlin.

Becker, W. (2005). ''The bh TCSPC Handbook.'' Beckher & Hickl GmbH.

Berezovsky, J., Mikkelsen, M. H., Gywat, O., Stoltz, N. G., Coldren, L. A., and Awschalom, D. D. (2006). *Science* **314,** 1916–1920.

Berezovsky, J., Mikkelsen, M. H., Stoltz, N. G., Coldren, L. A., and Awschalom, D. D. (2008). *Science* **320,** 349–352.

Besombes, L., Leger, Y., Maingault, L., Ferrand, D., Mariette, H., and Cibert, J. (2004). *Phys. Rev. Lett.* **93**(20), 207403.

Bracker, A. S., Stinaff, E. A., Gammon, D., Ware, M. E., Tischler, J. G., Shabaev, A., Efros, A. l. L., Park, D., Gershoni, D., Korenev, V. L., and Merkulov, I. A. (2005). *Phys. Rev. Lett.* **94**(4), 047402.

Brooke, P. G. (2007). *Phys. Rev. A* **75**(2), 022320.

Carter, S. G., Chen, Z., and Cundiff, S. T. (2007). *Phys. Rev. B* **76**(20), 201308.

Chapman, R. A., and Hutchinson, W. G. (1967). *Phys. Rev. Lett.* **18**(12), 443–445.

Charnock, F. T., and Kennedy, T. A. (2001). *Phys. Rev. B* **64**(4), 041201.

Chen, P., Piermarocchi, C., Sham, L. J., Gammon, D., and Steel, D. G. (2004). *Phys. Rev. B* **69,** 075320.

Childress, L., Gurudev Dutt, M. V., Taylor, J. M., Zibrov, A. S., Jelezko, F., Wrachtrup, J., Hemmer, P. R., and Lukin, M. D. (2006a). *Science* **314**(5797), 281–285.

Childress, L., Taylor, J. M., Sørensen, A. S., and Lukin, M. D. (2006b). *Phys. Rev. Lett.* **96**(7), 070504.

Clark, C. D., and Norris, C. A. (1971). *J. Phys. C: Sol. Stat. Phys.* **4**(14), 2223–2229.

Clark, S. M., Fu, K. M. C., Ladd, T. D., and Yamamoto, Y. (2007). *Phys. Rev. Lett.* **99,** 040501.

Cohen-Tannoudji, C., and Dupont-Roc, J. (1972). *Phys. Rev. A* **5,** 968–984.

Cohen-Tannoudji, C., and Reynaud, S. (1977). *J. of Phys. B* **10,** 345–363.

Combescot, M., and Betbeder-Matibet, O. (2004). *Solid State Commun.* **132,** 129–134.

Combescot, M., and Combescot, R. (1988). *Phys. Rev. Lett.* **61,** 117–120.

Damen, T. C., Via, L., Cunningham, J. E., Shah, J., and Sham, L. J. (1991). *Phys. Rev. Lett.* **67** (24), 3432–3435.

Dietl, T. (1994). ''Handbook on Semiconductors,'' Vol. 3B. North-Holland, Amsterdam.

Dutt, M. V., Gurudev, J., Cheng, J., Wu, Y., Xu, X., Steel, D. G., Bracker, A. S., Gammon, D., Economou, S. E., Liu, R. B., and Sham, L. J. (2006). *Phys. Rev. B* **74,** 125306.

Dutt, M. V., Gurudev, L., Childress, L., Jiang, L., Togan, E., Maze, J., Jelezko, F., Zibrov, A. S., Hemmer, P. R., and Lukin, M. D. (2007). *Science* **316**(5829), 1312–1316.

Dzhioev, R. I., Kavokin, K. V., Korenev, V. L., Lazarev, M. V., Meltser, B. Y., Stepanova, M. N., Zakharchenya, B. P., Gammon, D., and Katzer, D. S. (2002). *Phys. Rev. B* **66**(24), 245204.

Ebbens, A., Krizhanovskii, D. N., Tartakovskii, A. I., Pulizzi, F., Wright, T., Savelyev, A. V., Skolnick, M. S., and Hopkinson, M. (2005). *Phys. Rev. B* **72**(7), 073307.

Economou, S. E., Sham, L. J., Wu, Y., and Steel, D. G. (2006). *Phys. Rev. B* **74,** 205415.

Epstein, R. J. (2005). Controlled Interactions of Single Spins and Ensembles in Semiconductors. PhD thesis, University of California, Santa Barbara.

Epstein, R. J., Mendoza, F. M., Kato, Y. K., and Awschalom, D. D. (2005). *Nat. Phys.* **1,** 94.

Erlingsson, S. I., Nazarov, Y. V., and Fal'ko, V. I. (2001). *Phys. Rev. B* **64,** 195306.

Erwin, S. C., and Petukhov, A. G. (2002). *Phys. Rev. Lett.* **89**(22), 227201.

Farrier, R. G. (1969). *Solid State Commun.* **7,** 685.

Frey, T. h., Maier, M., Schneider, J., and Gehrke, M. (1988). *J. Phys. C: Sol. Stat. Phys.* **21**(32), 5539–5545.

Furdyna, J. K. (1988). *J. Appl. Phys.* **64**(4), R29–R64.

Gaebel, T., Domhan, M., Popa, I., Witmman, C., Neumann, P., Jelezko, F., Rabeau, J. R., Stavrias, N., Greentree, A. D., Prawer, S., Meijer, J., Twamley, J., *et al.* (2006). *Nat. Phys.* **2,** 408.

Gammon, D., Snow, E. S., Shanabrook, B. V., Katzer, D. S., and Park, D. (1996). *Phys. Rev. Lett.* **76,** 3005–3008.

Gammon, D., Efros, A. L., Kennedy, T. A., Rosen, M., Katzer, D. S., Park, D., Brown, S. W., Korenev, V. L., and Merkulov, I. A. (2001). *Phys. Rev. Lett.* **86**(22), 5176–5179.

Golovach, V. N., Khaetskii, A., and Loss, D. (2004). *Phys. Rev. Lett.* **93,** 016601–016604.

Gossard, A. C. (1986). *IEEE J. Quant. Electron.* **22**(9), 1649–1655.

Gottesman, D., and Chuang, I. L. (1999). *Nature* **402**(6760), 390–393.

Greilich, A., Wiemann, M., Hernandez, F. G. G., Yakovlev, D. R., Yugova, I. A., Bayer, M., Shabaev, A., Efros, A. l., Reuter, D., and Wieck, A. D. (2007). *Phys. Rev. B* **75**(23), 233301.

Guest, J. R., Stievater, T. H., Li, X., Cheng, J., Steel, D. G., Gammon, D., Katzer, D. S., Park, D., Ell, C., Thränhardt, A., Khitrova, G., and Gibbs, H. M. (2002). *Phys. Rev. B* **65,** 241310.

Gupta, J. A., Knobel, R., Samarth, N., and Awschalom, D. D. (2001). *Science* **292**(5526), 2458–2461.

Gurudev-Dutt, M. V., Cheng, J., Li, B., Xu, X., Li, X., Berman, P. R., Steel, D. G., Bracker, A. S., Gammon, D., Economou, S. E., Liu, R. B., and Sham, L. J. (2005). *Phys. Rev. Lett.* **94,** 227403–227404.

Hanson, R., Gywat, O., and Awschalom, D. D. (2006a). *Phys. Rev. B* **74**(16), 161203.

Hanson, R., Mendoza, F. M., Epstein, R. J., and Awschalom, D. D. (2006b). *Phys. Rev. Lett.* **97** (8), 087601.

Hanson, R., P Kouwenhoven, L., Petta, J. R., Tarucha, S., and Vandersypen, L. M. K. (2007). *Rev. Mod. Phys.* **79,** 1217.

Harrison, J., Sellars, M. J., and Manson Manson, N. B. (2004). *J. Lumin.* **107,** 245.

He, X. F., Manson, N. B., and Fisk, P. T. H. (1993). *Phys. Rev. B* **47**(14), 8816–8822.

Högele, A., Kroner, M., Seidl, S., Karrai, K., Atatüre, M., Dreiser, J., Imamoglu, A., Warburton, R. J., Badolato, A., Gerardot, B. D., and Petroff, P. M. (2005). *Appl. Phys. Lett.* **86,** 221905.

Imamoglu, A., Awschalom, D. D., Burkard, G., DiVincenzo, D. P., Loss, D., Sherwin, M., and Small, A. (1999). *Appl. Phys. Lett.* **83,** 4204–4207.

Isberg, J., Hammersberg, J., Johansson, E., Wikstrom, T., Twitchen, D. J., Whitehead, A. J., Coe, S. E., and Scarsbrook, G. A. (2002). *Science* **297**(5587), 1670–1672.

Jelezko, F., Gaebel, T., Popa, I., Domhan, M., Gruber, A., and Wrachtrup, J. (2004). *Phys. Rev. Lett.* **93**(13), 130501.

Joffre, M., Hulin, D., Migus, A., and Combescot, M. (1989). *Phys. Rev. Lett.* **62,** 74–77.

Karlik, I. Ya, Merkulov, I. A., Mirlin, D. N., Nikitin, L. P., Perel', V. I., and Sapega, V. F. (1982). *Sov. Phys. Solid State* **24,** 2022.

Kennedy, T. A., Colton, J. S., Butler, J. E., Linares, R. C., and Doering, P. J. (2003). *Appl. Phys. Lett.* **83**(20), 4190–4192.

Khaetskii, A. V., and Nazarov, Y. V. (2001). *Phys. Rev. B* **64,** 125316.

Khaetskii, A. V., Loss, D., and Glazman, L. (2002). *Phys. Rev. Lett.* **88,** 186802.

Kim, Y., Shon, Y., Takamasu, T., and Yokoi, H. (2005). *Phys. Rev. B* **71**(7), 073308.

Kitchen, D., Richardella, A., Tang, J. M., Flatté, M. E., and Yazdani, A. (2006). *Nature* **442** (7101), 436–439.

Koppens, F. H. L., Buizert, C., Tielrooij, K. J., Vink, I. T., Nowack, K. C., Meunier, T., Kouwenhoven, L. P., and Vandersypen, L. M. K. (2006). *Nature* **442**(7104), 766–771.

Kurtsiefer, C., Mayer, S., Zarda, P., and Weinfurter, H. (2000). *Phys. Rev. Lett.* **85**(2), 290–293.

Leger, Y., Besombes, L., Fernandez-Rossier, J., Maingault, L., and Mariette, H. (2006). *Phys. Rev. Lett.* **97**(10), 107401.

Li, J. B., and Wang, L. W. (2004). *Appl. Phys. Lett.* **84**(18), 3648–3650.

Li, Y. Q., Steuerman, D. W., Berezovsky, J., Seferos, D. S., Bazan, G. C., and Awschalom, D. D. (2006). *Appl. Phys. Lett.* **88,** 193126.

Liu, X., Prasad, A., Nishio, J., Weber, E. R., Liliental-Weber, Z., and Walukiewicz, W. (1995). *Appl. Phys. Lett.* **67**(2), 279–281.

Loubser, J., and van Wyk, J. A. (1978). *Rep. Prog. Phys.* **41,** 1201.

Manson, N. B., and McMurtrie, R. L. (2007). *J. Lumin.* **127,** 98.

Manson, N. B., Harrison, J. P., and Sellars, M. J. (2006). *Phys. Rev. B* **74**(10), 104303.

Meier, F., and Awschalom, D. D. (2005). *Phys. Rev. B* **71**(20), 205315–205319.

Meier, F., and Zakharchenya, B. P. (1984). Optical Orientation. Elsevier, Amsterdam.

Meijer, J., Burchard, B., Domhan, M., Wittmann, C., Gaebel, T., Popa, I., Jelezko, F., and Wrachtrup, J. (2005). *Appl. Phys. Lett.* **87**(26), 261909.

Merkulov, I. A., Efros, A. L., and Rosen, M. (2002). *Phys. Rev. B* **65**.

Mikkelsen, M. H., Berezovsky, J., Stoltz, N. G., Coldren, L. A., and Awschalom, D. D. (2007). *Nat. Phys.* **3,** 770–773.

Myers, R. C., Poggio, M., Stern, N. P., Gossard, A. C., and Awschalom, D. D. (2005). *Phys. Rev. Lett.* **95**(1), 017204.

Myers, R. C., Mikkelsen, M. H., Tang, J. M., Gossard, A. C., Flatte, M. E., and Awschalom, D. D. (2008). *Nat. Mater.* **7,** 203.

Nizovtsev, A. P., Kilin, S. Ya, Jelezko, F., Popa, I., Gruber, A., and Wrachtrup, J. (2003). *Phys. B* **340,** 106.

Nowack, K. C., Koppens, F. H. L., Nazarov, Yu. V., and Vandersypen, L. M. K. (2007). *Science* **318,** 1430–1433.

Ohno, H. (1998). *Science* **281**(5379), 951–956.

Papageorgiou, G., Chari, R., Brown, G., Kar, A. K., Bradford, C., Prior, K. A., Kalt, H., and Galbraith, I. (2004). *Phys. Rev. B* **69,** 085311.

Poggio, M., Myers, R. C., Stern, N. P., Gossard, A. C., and Awschalom, D. D. (2005). *Phys. Rev. B* **72**(23), 235313.

Pryor, C. E., and Flatté, M. E. (2006). *Appl. Phys. Lett.* **88,** 233108.

Rabeau, J. R., Reichart, P., Tamanyan, G., Jamieson, D. N., Prawer, S., Jelezko, F., Gaebel, T., Popa, I., Domhan, M., and Wrachtrup, J. (2006). *Appl. Phys. Lett.* **88**(2), 023113.

Rosatzin, M., Suter, D., and Mlynek, J. (1990). *Phys. Rev. A* **42,** 1839(R)–1841.

Rugar, D., Budakian, R., Mamin, J., and Chui, B. W. (2004). *Nature* **430,** 329.

Sakurai, J. J. (1994). ''Modern Quantum Mechanics,'' rev. edn. Addison-Wesley.

Salis, G., and Moser, M. (2005). *Phys. Rev. B* **72,** 115325.

Salis, G., Awschalom, D. D., Ohno, Y., and Ohno, H. (2001). *Phys. Rev. B* **64**(19), 195304.

Sapega, V. F., Brandt, O., Ramsteiner, M., Ploog, K. H., Panaiotti, I. E., and Averkiev, N. S. (2007). *Phys. Rev. B* **75**(11), 113310.

Schairer, W., and Schmidt, M. (1974). *Phys. Rev. B* **10**(6), 2501–2506.

Schneider, J., Kaufmann, U., Wilkening, W., Baeumler, M., and Köhl, F. (1987). *Phys. Rev. Lett.* **59**(2), 240–243.

Semenov, Y. G., and Kim, K. W. (2004). *Phys. Rev. Lett.* **92**, 026601–026604.

Slicter, C. P. (1990). ''Principles of Magnetic Resonance,'' 3rd edn. Springer.

Stegner, A. R., Boehme, C., Huebl, H., Stutzman, M., Lips, K., and Brandt, M. S. (2006). *Nat. Phys.* **2**, 835.

Stern, N. P., Myers, R. C., Poggio, M., Gossard, A. C., and Awschalom, D. D. (2007). *Phys. Rev. B* **75**(4), 045329.

Stievater, T. H., Li, X., Cubel, T., Steel, D. G., Gammon, D., Katzer, D. S., and Park, D. (2002). *Appl. Phys. Lett.* **81**(22), 4251–4253.

Suter, D., Klepel, H., and Mlynek, J. (1991). *Phys. Rev. Lett.* **67**, 2001–2004.

Tang, J. M., and Flatté, M. E. (2004). *Phys. Rev. Lett.* **92**(4), 047201.

Tang, J. M., Levy, J., and Flatté, M. E. (2006). *Phys. Rev. Lett.* **97**(10), 106803.

Unold, T., Mueller, K., Lienau, C., Elaesser, T., and Wieck, A. D. (2004). *Phys. Rev. Lett.* **92**, 157401.

Vandersypen, L. M. K., and Chuang, I. L. (2005). *Rev. Mod. Phys.* **76**(4), 1037–1069.

Warburton, R. J., Schäflein, C., Haft, D., Bickel, F., Lorke, A., Karrai, K., Garcia, J. M., Schoenfeld, W., and Petroff, P. M. (2000). *Nature* **405**, 926–929.

Wei, L., Kuo, P. K., Thomas, R. L., Anthony, T. R., and Banholzer, W. F. (1993). *Phys. Rev. Lett.* **70**(24), 3764–3767.

Wolf, S. A., Awschalom, D. D., Buhrman, R. A., Daughton, J. M., von Molnar, S., Roukes, M. L., Chtchelkanova, A. Y., and Treger, D. M. (2001). *Science* **294**(5546), 1488–1495.

Wu, Y., Kim, E. D., Xu, X., Cheng, J., Steel, D. G., Bracker, A. S., Gammon, D., Economou, S. E., and Sham, L. J. (2007). *Phys. Rev. Lett.* **99**, 097402.

Yakunin, A. M., Silov, A. Y. u., Koenraad, P. M., Wolter, J. H., Van Roy, W., De Boeck, J., Tang, J. M., and Flatté, M. E. (2004). *Phys. Rev. Lett.* **92**(21), 216806.

Zrenner, A., Butov, L. V., Hagn, M., Abstreiter, G., Böhm, G., and Weimann, G. (1994). *Phys. Rev. Lett.* **72**, 3382–3385.